Title: Immune–Vascular intercellular signalling coordinates tissue plasticity during adult muscle repair in *Drosophila*.

Authors: Nourhene Ammar[1], Olivier Josse[1], Aurélien Guillou[1], Jessica Perochon[2] and Hadi Boukhatmi[1]*

[1] Institut de Génétique et Développement de Rennes (IGDR), Université de Rennes, CNRS UMR6290, Rennes, France.

[2] Institute of Cancer Sciences−University of Glasgow, Wolfson Wohl Cancer Research Centre, Glasgow, UK.

* Corresponding author: hadi.boukhatmi@univ-rennes.fr

Summary

In skeletal muscle, immune and vascular responses are essential for regeneration, yet the cellular and molecular mechanisms that coordinate their activities to restore tissue function remain unclear. Here, using *Drosophila*, we uncover a multi-organ signaling program that integrates muscle fibers, macrophages, vascular-like tracheal cells, and the extracellular matrix (ECM) to drive adult skeletal muscle repair. Muscle injury induces rapid macrophage recruitment and secretion of the FGF-like ligand Branchless (Bnl), which activates FGF/FGFR signalling in tracheal cells and promotes their targeted expansion toward damaged muscle. Concomitantly, macrophages deposit ECM components on the damaged muscle, including Collagen IV, forming a localized microenvironment that restricts Bnl ligand diffusion and facilitates directed tracheal remodelling. Genetic disruption of macrophage-derived Bnl or macrophage-mediated ECM deposition abolishes tracheal remodeling and compromises muscle recovery. Together, these findings reveal a previously unrecognized immune muscle vascular program in which macrophages coordinate growth factor signalling and ECM organization to shape muscle microenvironment and preserve muscle function following acute damage.

Introduction

Effective tissue repair relies on precise communication and coordination across multiple cell types and tissue systems [1]. Skeletal muscle provides a prime example of this interdependent cellular network, as successful regeneration depends on tightly orchestrated interactions among diverse cell populations, including macrophages, muscle stem cells (MuSCs; also known as satellite cells), and the fibro/adipogenic progenitors (FAPs) [2, 3]. Following injury, infiltrating macrophages promote muscle regeneration by signalling to MuSCs and regulating their activation, proliferation, and differentiation [4, 5]. In parallel, extensive remodelling of both the vasculature and the extracellular matrix (ECM) is required to meet increased metabolic demands and provide structural support [6, 7]. Immune, vascular, and ECM-mediated responses are therefore critical to muscle regeneration; however, how these systems are mechanistically integrated *in vivo* to drive effective repair remains poorly understood. Addressing this question has been limited by the lack of experimental systems that enable to track and manipulate multiple interacting cell types *in vivo* during muscle repair.

Drosophila has emerged as a powerful *in vivo* model for dissecting multi-organ communication during regeneration, owing to its capacity to combine precise genetic manipulation with high-resolution imaging [8]. As in vertebrates, adult *Drosophila* indirect flight muscles (IFMs) harbor MuSCs that support muscle maintenance and have been implicated in regenerative responses following injury [9-11]. The IFMs muscles are organized into six stereotypically arranged bilateral pairs within the adult thorax [12]. Studies, including our own, have shown that macrophage-like immune cells, termed hemocytes, populate the IFMs under homeostatic conditions [9, 13]. In addition to hemocytes, the IFMs are infiltrated by a sophisticated network of air-filled tracheal cells, which function analogously to the vertebrate vascular and respiratory systems by ensuring tissue oxygenation [14, 15]. While tracheal branching has been extensively characterized at the morphological, cellular, and genetic levels during development [16, 17], recent work has revealed that adult tracheal networks retain a remarkable capacity for dynamic remodelling in response to tissue damage, including during regeneration of the adult gut [18-20]. Finally, IFMs are ensheathed by a specialized basement membrane enriched in conserved ECM components, which

provide structural integrity and mechanical support to the contractile apparatus [15, 21]. These features provide an *in vivo* context in which interactions between muscle fibres, immune cells, vascular-like trachea, and the ECM can be explored during muscle repair.

We show that muscle damage triggers rapid and sustained hemocyte recruitment, which is required for targeted tracheal remodelling through FGF/FGFR signalling, enabling selective recognition and support of damaged fibers. In parallel, hemocytes deposit ECM components around injured fibres, which spatially confine FGF-like ligand and promote tracheal recruitment. Disrupting tracheal remodelling or hemocyte-mediated ECM delivery compromises muscle performance after injury, revealing an immune–muscle–vascular signalling module that couples metabolic support to ECM organization to preserve muscle function.

Results

Hemocytes are recruited to the injured adult flight muscle

Accurate analysis of muscle injury responses requires a robust molecular readout that distinguishes damaged muscle fibers from adjacent intact muscles. Although *Drosophila* is one model for studying muscle repair, it lacks molecular markers that specifically identify injured muscle fibers. In vertebrates, re-expression of embryonic Myosin Heavy Chain (MyHC-emb) in damaged fibers is a common marker of muscle injury and regeneration [22]. To assess whether Myosin Heavy Chain (Mhc) expression could similarly serve as an indicator of muscle damage in *Drosophila*, we analysed its expression following injury. Our results show that Mhc expression is drastically upregulated in injured muscles (Figure 1 A-F) and inversely correlated with the downregulation of Mef2, providing a robust molecular readout of muscle damage (Figure S1 A-B''). This upregulation persists for at least 20 days post-injury (DPI) (Figure S2 C-L). In *Drosophila*, several Mhc isoforms are generated via alternative splicing of a single *Mhc* gene [23]. To determine which isoform respond to injury, we analysed the expression of various GFP-tagged Mhc isoforms [23, 24]. Only the shorter adult Mhc isoforms-K, L, and M-were upregulated in response to muscle damage (Figure S1 C-E''). To rule out the possibility that Mhc upregulation is an artifact

of the injury method used, we examined its expression in *Naa30A* mutants, which exhibit developmental defects in flight muscles and spontaneous muscle detachment in eight-day-old adults, along with loss of nuclear Mef2 expression [25]. In these mutants, Mhc upregulation coincided with Mef2 downregulation (Figure S1 F-G''), further supporting Mhc as a reliable marker of muscle damage in *Drosophila*.

The contribution of the hemocytes in IFMs repair remains largely unexplored. To address this, we started by tracking these cells at various time points after injury using the hemocytes reporters Peroxidasin (*Pxn*) (Figure 1 A-C'') and Hemolectin (*Hml*) (Figure S1 H-I''). Co-staining for these markers and Mhc revealed extensive recruitment of hemocytes to the injured muscle fibers (Figure 1 A-C'; Figure S1 H-I''). Notably, while Pxn+ hemocytes persist at the injured muscle for at least 5 DPI, Hml+ hemocytes enrichment declines over time (Figure 1 G), highlighting the heterogeneity of the adult hemocyte population, consistent with previous findings [26]. To further characterize the hemocytes recruitment dynamics, we examined the zinc finger homeodomain transcription factor Zfh1 reporter (*Enh3-Gal4 > UAS-mCD8GFP*), another hemocytes marker [9, 27] (Figure 1 D-F''). Enh3+ hemocytes exhibited recruitment kinetics similar to Pxn+ cells (Figure 1 G). Importantly, at 5 DPI all Pxn+ cells were also Enh3+, whereas only a subset of Pxn+ cells were Hml+ (Figure 1 G' and Figure S1 H-K'''). None of the recruited Enh3+ hemocytes expressed the myogenic marker Mef2 (Figure S1 L'-M'). To confirm that hemocytes recruitment is a response to muscle damage, we analyzed *Naa30A* mutants. Consistently, we observed a selective recruitment of Enh3+ hemocytes to injured muscle fibers, identified by high Mhc expression and the loss of Mef2 nuclear expression (Figure 1 H-I'''). Altogether, these data show that adult hemocytes are rapidly and specifically recruited to injured muscle fibers, with distinct subpopulations displaying differential persistence over time.

Hemocytes recruitment coordinates with tracheal remodelling following muscle injury

We observed that hemocytes are closely associated with muscle tracheal cells under homeostatic conditions (Figure 2A–A'). Previous studies have shown that adult tracheal cells can undergo dynamic remodeling and extend new branches toward damaged regions to support gut regeneration [18, 19]. We therefore asked whether

129 tracheal remodeling also occurs in response to IFMs injury and whether this process
130 involves intercellular communication between tracheal cells and hemocytes. Our
131 analysis revealed that muscle damage, whether caused by physical injury or in
132 *Naa30A* mutant animals, leads to a significant increase in tracheal coverage of the
133 injured fiber (Figure 2 B-D and Figure S2 A-B'). The invasion is directed toward the
134 injury site, with the highest branching density close to the damaged area and
135 progressively decreasing with distance from the injury (Figure 2 E). We further
136 observed that hemocytes remain spatially close to the tracheal branches, even under
137 injured conditions, suggesting sustained interactions between these two cell types
138 during the muscle damage response (Figure 2 C'').

139 To further investigate the tracheal response to injury, we focused on terminal tracheal
140 cells (TTCs), specialized branches of the tracheal system known for their structural
141 plasticity and ability to invade tissues, including muscle fibers, to deliver oxygen [14,
142 15, 28]. TTCs can be reliably identified by their distinctive morphology and the
143 expression of the transcription factor Serum Response Factor (dSRF) (Figure 2 F-F'
144 and J-J'). We visualized TTCs by expressing membrane-bound GFP under the control
145 of dSRF-Gal4 (*dSRF-Gal4 > UAS-mCD8GFP*) (Figure 2 G-H'''). We observed a high
146 density of TTCs within injured muscle fibers, with the highest concentration near the
147 injury site (Figure 2 H-H''' and I). Orthogonal views showed that the recruited trachea
148 are found not only on the muscle surface but also extend branches into the injured
149 fibers (Figure 2 G'''-H'''), consistent with the atypical muscle-tracheal organization
150 optimized to deliver oxygen deep within the muscle, directly to sites of high metabolic
151 demand [14, 15]. Labelling TTCs nuclei with anti-dSRF confirmed the significant
152 enrichment of dSRF+ nuclei along the injured fibers comparing to the uninjured
153 muscles (Figure 2 K-L'' and M). The tracheal enrichment at the injured muscle results
154 from TTCs branching and recruitment rather than proliferation, as no PH3+ cells were
155 detected in the muscle trachea cells (Figure 2 K'''-L'''). Altogether, these data indicate
156 that tracheal cells respond to muscle injury and target specifically the damaged fiber.

157 We found that tracheal enrichment around injured muscles persists throughout the
158 repair process and is still present 20 days post-injury (Figure S2 C-K' and N), a stage
159 at which muscle healing is expected to be complete [10, 11]. A comparison of
160 hemocyte recruitment kinetics with tracheal coverage density revealed that hemocyte

recruitment precedes tracheal coverage of the injured fibers (Figure S2 M and N), raising the possibility of an interplay between the two-cell population in supporting the injured muscle fiber.

Tracheal invasion of injured muscle fibers is triggered by local hypoxia

The tracheal recruitment to injured muscle fibers (Figure 2) suggests a critical oxygen demand of the damaged muscle. If this is the case, local hypoxia within injured fibers could serve as a key cue for tracheal attraction and directional growth toward the site of injury, as seen in other physiological contexts [29]. To assess oxygen variations within the injured muscle, we first used the Synthetic HRE (Hypoxia response element) nuclear sensor (SyHREns), a hypoxia reporter that serves as a proxy for evaluating intracellular oxygen fluctuations [30]. In normal condition, the SyHREns was found to be expressed in some TTCs, identifiable by both their triangular shape and expression of dSRF (Figure 3 A-A''). Importantly, we observed a pronounced enrichment of SyHREns-positive cells surrounding injured muscle fibers, in close proximity to the recruited tracheal branches (Figure 3 B-D''). The high number of SyHREns+ cells around the injured fibers remained stable for at least 20 DPI (Figure 3 E), indicating that local hypoxia persists in parallel with the sustained tracheal remodelling observed over the same period.

Hypoxia-induced tracheogenesis is controlled by the transcription factor Similar (Sima) -the *Drosophila* homolog of hypoxia-inducible factor-1α (HIF-1α)- a central regulator of hypoxic and angiogenic responses [29]. Accordingly, silencing *sima* in TTCs severely decreased tracheal expansion towards the injured fibers (Figure 3 F-I). Bnl is a well-established downstream effector of hypoxic signalling, deposited locally on hypoxic tissues to promote tracheal attraction [29]. We therefore hypothesised that if the injured muscle undergoes hypoxia, Bnl should accumulate locally at the damaged fiber to facilitate tracheal remodelling. Analysing the expression of an endogenously tagged *Bnl::GFP*^{endo} allele [31] revealed marked enrichment of Bnl at injured muscle fibers compared to adjacent intact ones (Figure 3 J-K''' and L). Altogether, these data suggest that muscle damage induces local muscle oxygen starvation, which in turn drives tracheal cell recruitment to the injured tissue.

192 **Hemocytes deposit FGF-like ligand Bnl at injured muscles to mediate tracheal**
193 **recruitment**

194 During both embryonic and post-embryonic stages, tracheal guidance is regulated in
195 a dose-dependent manner by local Bnl concentrations [29]. In adult flight muscle
196 development, muscle-tracheal connections are established through the action of Bnl,
197 which is secreted by muscle fibers and acts in a paracrine manner by binding to its
198 receptor, FGFR/Breathless (Btl), expressed on tracheal cells [14]. The observed
199 enrichment of Bnl in injured muscles (Figure 3 J-L) raises two key questions: Is Bnl/Btl
200 signaling functionally involved in directing tracheal recruitment to damaged fibers? If
201 so, what is the source of Bnl enrichment on the injured fibers? To begin addressing
202 these questions, we conditionally overexpressed Bnl in a restricted subset of adult
203 muscle fibers using the flip-out system combined with a regionally expressed driver
204 (Figure S3 A-C and Materials and Methods section). This targeted overexpression was
205 sufficient to recruit tracheal cells to the ectopic Bnl-expressing regions (Figure 4 A-C'),
206 and the extent of this recruitment depended on the duration of Bnl expression:
207 prolonged expression (5 days) triggered more extensive tracheal remodelling than
208 short-term expression (24 hours). These findings showed that the adult tracheal
209 system remains responsive to elevated Bnl levels in the IFMs, supporting the
210 hypothesis that Bnl/Btl signalling directs tracheal pathfinding in response to muscle
211 injury.

212 We next sought to identify the cellular source responsible for Bnl accumulation in
213 injured muscle fibers. Under wild-type conditions, Bnl::GFP^{endo} signal was detected in
214 hemocytes, tracheal cells, and IFMs (Figure S3 D-D'). However, since Bnl is a diffusible
215 protein, these observations alone cannot distinguish between cells that produce Bnl
216 and those that merely take it up. To address this, we used the *Bnl-lacZ* transcriptional
217 reporter, which revealed active *bnl* expression in hemocytes, adult IFMs, and TTCs,
218 confirming that these cell types are bona fide sources of Bnl under normal conditions
219 (Figure S3 E-F'). Given that canonical Bnl/Btl signalling operates in a paracrine
220 manner, injured muscles and hemocytes emerge as the most plausible sources of
221 injury-induced Bnl accumulation. To distinguish between these two possibilities, we
222 examined *Bnl-lacZ* expression following injury. Surprisingly, we found that injured fibers
223 nuclei lacked *Bnl-lacZ* activity, whereas neighboring uninjured fibers retained its

224 expression (Figure 4 D-E''). These findings indicate that the injured muscle fibers
225 themselves do not contribute to the localized Bnl accumulation after injury and suggest
226 that the source of Bnl is extrinsic to the damaged tissue.

227 By contrast, we observed a marked enrichment of Bnl::GFP^{endo} signal surrounding
228 Pxn+ hemocytes recruited to the damaged fibers, suggesting that hemocytes are
229 responsible for depositing Bnl along injured muscles (Figure 4 F-G''). To assess the
230 functional contribution of hemocyte-derived Bnl to tracheal invasion, we selectively
231 silenced *bnl* in hemocytes using either the *Enh3-Gal4* or *HmlΔ-Gal4* drivers. While
232 hemocyte recruitment to injured muscles was unaffected, *bnl* knockdown significantly
233 reduced tracheal invasion into damaged fibers compared with controls (Figure 4 H-J''
234 and K; Figure S3 G-I'' and J). This signalling logic between the two cell types aligns
235 with their close anatomical association under homeostatic conditions (Figure 2 A-A'
236 and [13].

237 Given the critical role of the tracheal system in supporting tissue function [16], we next
238 asked whether hemocyte-mediated tracheal recruitment via Bnl is required to maintain
239 muscle flight performance after injury. To test this, we performed flight assays on
240 uninjured controls, injured flies, and injured flies in which *bnl* was specifically depleted
241 from hemocytes. Injured flies exhibited reduced flight capability compared with
242 uninjured controls (Figure 4 L-L'). Importantly, flies lacking hemocyte-derived Bnl
243 showed an even greater impairment in flight, underscoring the functional importance
244 of this signalling in promoting tracheal remodelling and preserving muscle performance
245 following injury (Figure 4 M).

246 **The receptor FGFR/Btl is essential for injury-induced tracheal guided outgrowth**

247 The finding that Bnl orchestrates tracheal morphogenesis in response to muscle
248 damage suggested in turn that it activates its receptor Btl, on tracheal cells, thereby
249 driving guided outgrowth and branching. To investigate this, we examined Btl
250 expression in adult flight muscles using an endogenously tagged *Btl::cherry^{endo}* allele,
251 which faithfully reports Btl expression [31]. Btl::cherry^{endo} was detected along tracheal
252 branches under homeostatic conditions and within tracheal structures invading the
253 injured muscle (Figure 5 A-B''). To complement this approach, we expressed a
254 membrane-tethered GFP (mCD8-GFP) under the control of a *Btl-Gal4* driver (Figure 5

255 C-E'). While Btl::cherry^{endo} reflects consistent endogenous expression, *Btl-Gal4* drives
256 a more heterogeneous pattern across tracheal cells (Figure 5 C-C'). Nevertheless, we
257 observed a striking accumulation of tracheal branches labelled by *Btl-Gal4* at injured
258 muscles, reinforcing that Btl-expressing tracheal cells are actively recruited to
259 damaged fibers (Figure 5 D-E'). We then tested whether Btl function is required for
260 proper tracheal pathfinding. To this end, *btl* was specifically silenced in tracheal cells
261 using either *dSRF-Gal4* or *Btl-Gal4* drivers (Figure 5 F-I''). In both cases, tracheal
262 invasion into injured fibers was significantly impaired compared to the control (Figure
263 5 J). Notably, the impairment was more pronounced with *dSRF-Gal4*, consistent with
264 its more uniform expression in terminal tracheal cells (Figure 2 F-F') compared with
265 *Btl-Gal4* (Figure 5 C-C'). Together, these findings show that the Bnl/Btl signalling axis
266 plays a pivotal role in guiding tracheal remodelling after muscle damage. While Btl
267 expression is restricted to tracheal cells, localized Bnl secretion from hemocytes at the
268 damaged fiber refines tracheal pathfinding, ensuring precise and targeted tracheal
269 invasion into injured muscle (Figure 5 K).

270 **Hemocyte-derived ECM retains Bnl ligand at injured muscles**

271 Although Bnl is a diffusible molecule, we observed that it is specifically retained at the
272 injured fiber (Figure 3 K'-K''), raising the question of what restricts its spatial
273 distribution. Previous study has shown that Collagen IV, a principal structural
274 component of the muscle ECM, is critical for retaining diffusible signals within defined
275 tissue regions [32]. We therefore hypothesized that ECM components may similarly
276 act to confine Bnl to the damaged fiber. Hemocytes are known to be major producers
277 of ECM components during both *Drosophila* development and post-developmental
278 stages [33, 34], suggesting they could supply Collagen IV in response to adult muscle
279 injury. To test this, we analysed Collagen IV distribution in adult flight muscles using
280 the Vkg::GFP line (Figure 6 A-B''). Under homeostatic conditions, we observed a basal
281 level of Vkg::GFP surrounding muscle fibers and along tracheal branches (Figure 6
282 A'), and we found that hemocytes express Collagen IV (Figure 6 A''). Five days after
283 injury, Vkg::GFP was markedly enriched in damaged fibers compared with intact
284 muscles and uninjured controls (Figure 6 A-B and A''-B''). To further assess the
285 relationship between hemocytes and ECM remodeling, we examined Collagen IV
286 distribution across multiple time points post-injury (1-20 DPI) and compared this to

287 hemocyte recruitment dynamics (Figure 6 C-D'' and Figure S4 A-F). Collagen IV
288 accumulation closely correlated with the presence and distribution of hemocytes.
289 Notably, regions where hemocytes were evenly distributed along the injured fiber
290 displayed stronger and more uniform Vkg::GFP signal. Together, these data suggest
291 that hemocytes are, at least in part, a source of Collagen IV within injured muscle
292 tissue.

293 To test whether hemocyte-supplied Collagen IV is necessary for Bnl retention at injured
294 fibers, we knocked down Collagen IV specifically in hemocytes and assessed
295 Bnl::GFP^{endo} localization (Figure 6 E-F'' and Figure S4 G-J). In control flies, Bnl signal
296 was strongly enriched along the injured fiber; however, this enrichment was
297 significantly reduced following hemocyte-specific Collagen IV depletion (Figure 6 E-F''
298 and G). Importantly, hemocytes recruitment to damaged fibers was not affected by
299 Collagen IV depletion (Figure S4 G-J), indicating that Collagen IV is not required for
300 immune cell recruitment to injured fibers. These data show that hemocyte-derived
301 Collagen IV is required to spatially confine Bnl to the damaged fibers (Figure 6 H).

302 We next asked whether loss of Bnl confinement following hemocyte-specific Collagen
303 IV depletion affects tracheal remodelling after muscle injury. Absolute tracheal
304 enrichment at injured fibers was comparable between control and Collagen IV–
305 depleted conditions (Figure S4 K). However, the ratio of tracheal coverage at injured
306 muscles relative to neighbouring intact muscles was significantly reduced when
307 Collagen IV was depleted in hemocytes (Figure S4 H'''-H'''', I'''-I'''' and K'). These data
308 indicate that loss of ECM induces Bnl signal to spread beyond the injury site, thereby
309 provoking non-specific tracheal remodelling in adjacent, intact muscles.
310

311 **Hemocyte-derived SPARC supports Collagen IV deposition, tracheal**
312 **remodleling and muscle recovery**

313 Incorporation of Collagen IV into the extracellular matrix (ECM) requires accessory
314 molecules for proper deposition and stabilization. SPARC is a collagen-binding
315 glycoprotein essential for Collagen IV diffusion, stabilization, and incorporation into
316 basement membranes [35, 36]. We therefore investigated whether hemocytes also
317 supply SPARC during muscle repair. We first examined SPARC localization in

hemocytes associated with adult IFMs. Hemocytes, identified using *Enh3-Gal4* driver, were positive for SPARC (Figure 6 I-I'). Importantly, following muscle injury, SPARC levels were elevated along the injured fiber compared with controls, mirroring the distribution of Collagen IV (Figure 6 I-J'). These observations suggest that SPARC is locally produced by hemocytes in adult muscle. To further confirm the cellular origin of SPARC enrichment in injured muscles, we employed the SPARC-Gal4 driver, a Gal4 trap line inserted into the endogenous SPARC locus, to drive membrane-targeted RFP (myr-RFP) expression in flies also carrying a BM40-SPARC-GFP fosmid reporter (Figure 6 K-L' and Figure S4 L-M'). This dual-reporter approach allowed simultaneous visualization of SPARC (via BM40-SPARC-GFP) and identification of SPARC-producing cells (via SPARC-Gal4 > myr-RFP). In uninjured muscle, BM40-SPARC-GFP and SPARC-Gal4-driven myr-RFP were co-expressed in hemocytes. Following injury, BM40-SPARC-GFP was broadly enriched along the damaged fiber, resembling endogenous SPARC protein, whereas SPARC-Gal4 activity remained restricted to hemocytes and was not detected in muscle nuclei (Figure 6 L-L' and Figure S4 M-M'). Together, these data demonstrate that recruited hemocytes are the primary source of SPARC at injured muscle fibers. We then tested whether hemocyte-derived SPARC is required for Collagen IV enrichment and tracheal remodelling. Depletion of SPARC specifically in hemocytes was sufficient to prevent both Collagen IV accumulation and tracheal remodelling at the injured fiber (Figure 6 M-N'' and O-P). Finally, to evaluate the functional importance of SPARC in the muscle repair process, we performed flight assays and found that injured flies lacking hemocyte-derived SPARC exhibited significantly reduced flight ability compared with controls (Figure 6 Q). Altogether, these results show that hemocyte-derived SPARC is essential for ECM assembly, tracheal remodelling, and functional recovery following muscle injury. They also highlight that hemocytes act as multifunctional signalling hubs, simultaneously delivering trophic, structural, and guidance cues required to coordinate efficient muscle repair.

Discussion

Tissue repair requires the coordinated integration of immune, vascular, and structural responses, yet how these processes are mechanistically linked following muscle damage remains poorly understood. Here, we identify a signalling program in which hemocytes link muscle damage to vascular remodelling and extracellular matrix organization. We show that hemocytes respond to injury by locally delivering the FGF ligand Branchless to guide tracheal outgrowth toward damaged muscle, while simultaneously supplying extracellular matrix components, both of which are required for muscle maintenance after injury. Together, these findings indicate that hemocytes play a central role in organizing the regenerative microenvironment in adult *Drosophila* muscle (Figure 7).

Immune-derived FGF acts as an intercellular signalling cue to coordinate vascular remodelling during muscle repair

FGF signalling contributes to multiple aspects of vertebrate myogenesis and muscle regeneration [37-40]. For example, FGF2 stimulates myoblasts proliferation while suppressing differentiation *in vitro*, whereas FGF6 is required to maintain full regenerative capacity and MuSC pool size [41, 42]. However, whether FGF signalling also mediates vascular remodelling during vertebrate muscle repair, as it does in other regenerative contexts, remains unclear. One explanation for this gap may be the extensive functional redundancy of the vertebrate FGF family, which comprises multiple ligands with overlapping expression patterns and signalling activities. This redundancy complicates precise genetic dissection of individual FGF functions during regeneration. Moreover, the cellular sources of FGF ligands during muscle regeneration remain poorly defined [42], further limiting targeted genetic ablation strategies.

Here, we show that following muscle damage, hemocytes are rapidly recruited to and spread over the injured muscle surface, where they secrete the FGF ligand Branchless (Bnl) to promote localized tracheal outgrowth and precise branch targeting (Figure 7). This mode of immune-driven FGF delivery contrasts with the prevailing model in which the tissue requiring vascular or tracheal infiltration is itself thought to produce the FGF signal [29, 43]. The identification of a non–cell-autonomous source of FGF during

383 muscle repair is therefore unexpected and raises an important question: why does the
384 injured muscle fiber not itself express Bnl to attract tracheal branches? One possible
385 explanation is the need to tightly restrict tracheal growth. Bnl is a potent
386 chemoattractant, and its widespread expression by muscle fibers could lead to
387 excessive or ectopic tracheogenesis, resulting in inappropriate branch recruitment and
388 disruption of normal tracheal network architecture. In contrast, hemocytes are
389 comparatively sparse and become selectively localized to damaged regions, enabling
390 the spatially restricted secretion of Bnl. Such targeted delivery would ensure that
391 tracheal remodelling occurs specifically at sites of injury, where oxygen delivery and
392 tissue repair are most acutely required.

393 ***Local ECM delivery optimizes directed vascular outgrowth during muscle repair.***

394 The ECM is essential for muscle integrity and function [44]. However, its role in muscle
395 regeneration—particularly how its remodelling is coordinated with other cellular
396 processes during muscle repair—remains incompletely understood. In vertebrates,
397 fibro-adipogenic progenitors (FAPs) are the principal source of ECM within muscle
398 tissue [45]. *Drosophila* lack a dedicated FAP population. During development,
399 hemocytes are a major source of ECM components in flies [33, 46]. Here, we show
400 that adult hemocytes also produce key ECM components, including Collagen IV and
401 SPARC, that are required for muscle repair. These findings suggest that *Drosophila*
402 hemocytes share functional similarities with mammalian FAPs and may compensate
403 for their absence, pointing to an evolutionarily flexible strategy for muscle regeneration
404 in organisms with fewer specialized cell types. Moreover, we find that hemocyte-
405 derived ECM forms a specialized local microenvironment in which FGF distribution is
406 spatially constrained, thereby directing efficient vascular growth toward damaged
407 muscle. Whether the ECM physically interacts with FGF or instead acts primarily as a
408 diffusion barrier remains to be determined. Overall, these findings provide a
409 mechanistic example of how extracellular matrix remodelling is coordinated with
410 vascular remodelling to support muscle repair.

411 ***Do Drosophila repair or regenerate their flight muscles?***

412 The IFMs generate the high-frequency wing beats that enable flight, a behavior
413 essential for predator avoidance, foraging, and mating. Given their vital function, IFMs

must be maintained in optimal condition to ensure sustained performance throughout the animal's lifespan. This need for resilience is also underscored by the observation that over 30% of wild-caught flies exhibit physical injuries, frequently located in the thorax and abdomen [47]. Although a rare population of satellite-like cells has been identified in adult flies, the regenerative capacity of adult *Drosophila* muscles remains debated [48]. A major limitation has been the lack of appropriate molecular markers to monitor both muscle regeneration and muscle stem cell (MuSC) activity. In our study, we identified a specific isoform of the Myosin Heavy Chain (Mhc) that is consistently upregulated in damaged fibers. However, unlike in vertebrates, where MyHC-emb levels return to baseline following regeneration, Mhc expression in *Drosophila* remains elevated even 20 days post-injury (Figure S2). This makes Mhc a sensitive marker for identifying injury, but less useful for assessing complete muscle recovery. Adult MuSCs have been identified via the transcription factor Zfh1/ZEB and its reporter Enh3 [9, 10], the only presently known marker for these cells. Zfh1 is required for MuSCs maintenance, an equivalent role of ZEB was subsequently shown in mice [49]. Interestingly, both Zfh1 and ZEB are expressed in the muscle associated immune cells [9, 49]. In our study, we found that following muscle injury, 100% of the cells recruited to damaged fibers are both Enh3^{+} and Pxn^{+} (a plasmatocytes marker), while being negative for the muscle-specific marker Mef2 (Figure S1 L-M'). This strongly suggests that hemocytes are the predominant, if not exclusive cell population migrating to injured muscle. These findings suggest that adult *Drosophila* flight muscles possess limited intrinsic regenerative capacity and may instead rely on compensatory mechanisms such as increased oxygenation through tracheal remodelling and structural reinforcement via extracellular matrix (ECM) deposition-to cope with muscle damage. This is consistent with the broader idea that short-lived species prioritize immediate survival over long-term regenerative investment [50]. In such organisms, evolution favors fast and efficient repair mechanisms that support rapid recovery and fitness over complex, energy-intensive regeneration programs.

448 ## Materials and Methods

449 ### *Drosophila melanogater* strains and genetics

450 All *Drosophila melanogaster* stocks were grown on standard medium at 25°C. The
451 following stains were used: w^{118} as wild type (wt), *Pxn-RFP* [51], *HmlΔ-Gal4*
452 (BL#30140), *Enh3-Gal4* [9], *Mhc-Iso-K, L, M (fTRG500)* and *Mhc-Iso-A, F, G*
453 *(fTRG519)* [24], *weeP26* [23], *Bnl::GFP*^{endo} *and Btl::cherry*^{endo} [31], *Bnl-LacZ*
454 (BL#11704), , *dSRF-GAL4* (BL#25753), *Btl-Gal4* (BL#78328), *UAS-Btl*^{RNAi}
455 (BL#435544), *UAS-Bnl*^{RNAi} (BL#34572), *UAS-Bnl::GFP* [52], *Vkg::GFP* (BL#98343),
456 *BM40-SPARC-GFP* (Sarov et al., 2016), *SME-Gal4* (VT 0576871), *UAS-H2B-RFP*
457 [53], *UAS-mCD8GFP* (BL#5137), *UAS-myr-mRFP* (BL#7118), SyHREns [30], *UAS-*
458 *Sima*^{RNAi} (BL#26207), *SPARC-Gal4* (BL#77473), *UAS-SPARC*^{RNAi} (BL#40885), *UAS-*
459 *Vkg*^{RNAi} (BL#50895). *Naa30A* deletion males were obtained from crosses between
460 *Naa30A*$^{\Delta 74}$*/FM0* females and either UAS-mCD8GFP; Enh3-Gal4 (Figure 1) or Mhc-
461 Iso-K, L, M (Figure S1) males. RNAi experiments were carried out at 29°C. To achieve
462 temporal control of gene expression in adult tissues, the tubGal80^{ts} was employed,
463 allowing restriction of Gal4 activity to a specific time window. Fly crosses were initially
464 maintained at 18°C, and after adult eclosion, the progenies were transferred to 29°C,
465 where they remained until dissection. An exception was made for the Bnl knockdown
466 experiments shown in Figure 4 J-J'', which were performed without the tubGal80^{ts}
467 transgene.
468

469 **Generation of SME-FRT-stop-FRT-Gal4 fly line and flip-out induction procedure.**

470 SME (Shavenbaby Muscle Enhancer) is one of several enhancers of the *shavenbaby*
471 gene (VT057071-Gal4). It is active in larval muscle progenitors (AMPs) (Figure S3 A-
472 A') and remains active in a subpopulation of localized muscle nuclei in the adult indirect
473 flight muscles (IFMs) (Figure S3 B-B'). To generate the SME-FRT-stop-FRT-Gal4
474 construct, the cis-regulatory element from the original *shavenbaby* enhancer construct
475 was used to replace the *pAct* promoter in the pAct-FRT-stop-FRT3-FRT-FRT3-Gal4
476 vector (Addgene plasmid #52889). The resulting construct was integrated into the attP
477 site at cytological location 51D on chromosome II via embryo injection into vas-int; attP-
478 51D flies. To induce localized overexpression of Bnl::GFP in adult IFM nuclei, hsflp;
479 FRT-SME-stop-FRT-Gal4/CyO; tubGal80^{ts} females were crossed to UAS-Bnl::GFP

480 males. Progeny were raised at 18°C and subjected to a 2-hour heat shock at 37°C in
481 young adulthood (Figure 4 A-C').

482 **Immunohistochemistry and confocal microscopy**
483
484 Preparation and immunofluorescence of wing discs and adult muscles were performed
485 as previously described in [54]. The following primary antibody were used: Chicken
486 anti-βGal (1:100, Abcam, ab9361), Chicken anti-GFP (1:300, Abcam, ab13970),
487 Mouse anti-Mhc (1:200, DSHB, 3E8-3D3-s) , Mouse anti-dSRF (1:20, a gift from Mark
488 A. Krasnow, Stanford university California , USA), Rabbit anti-Mef2 (1:500 , DSHB,
489 Mef2-p), Rabbit anti-PH3 (1:100, Cell Signaling Technology, #9713), Rabbit anti-
490 SPARC (1:500, a gift from Maurice Ringuette, University of Toronto, Canada), Rabbit
491 anti-Zfh1 (1:5000, a gift from Ruth Lehmann, New York, USA), Rat anti-RFP (1:800,
492 Chromotek, 5F8-20), Alexa-conjugated Phalloidin (1:200, Thermo fisher scientific life
493 technologies).
494
495 **Induction of flight muscle injury**
496
497 Flight muscle injury was induced following previously described protocol [55]. Adult
498 flies (2-3 days post-eclosion) were anesthetized and positioned laterally under a
499 stereomicroscope. A single, localized stab wound was inflicted manually using a fine
500 stainless-steel needle (Minutien Pins, 0.1 mm diameter; #26002–10) to minimize tissue
501 damage and avoid extensive injury. Age-matched, uninjured flies served as controls.
502
503 **Flight assay**

504 Flight ability was assessed using a 1-m-long cylindrical flight column internally lined
505 with paper coated with a thin layer of glue. The adhesive sheet was divided evenly into
506 three longitudinal sections corresponding to the Top**,** Middle, and Bottom regions of
507 the tube (Figure 4L). For each experimental condition, an equal number of flies
508 (approximately 20–30) was released into the tube. After all flies had landed, the paper
509 was removed, flattened, and imaged for analysis.

510 Image quantification was performed semi-automatically using a custom R script, Fly-
511 Spy (available at https://github.com/Olivier-Josse/Fly-spy). Images were first

converted to grayscale and digitally divided into the three predefined regions. High-intensity spots corresponding to individual flies were identified by applying a manually adjusted threshold to ensure accurate segmentation. The number of flies detected in each region was quantified and expressed as a percentage of the total recovered flies. The distribution of flies across the three regions—reflecting high, intermediate, or low/absent flight ability—was compared between experimental conditions using a chi-square (χ^2) test. Results are presented as stacked bar histograms

Microscopy and data analysis

Samples were imaged using a Leica SP8 microscope (BIOSIT, University of Rennes) at 20×, 40×, or 63× magnification and a resolution of 1024×1024 pixels. Images were processed with ImageJ and assembled using Adobe Illustrator. To quantify fluorescence intensity, all samples were processed and analyzed in parallel under identical conditions. Confocal images were acquired using the same laser settings across all samples. Sum slice projections were generated from each confocal stack. Regions of interest (ROIs) were manually defined based on protein expression, and mean fluorescence intensities were measured within each ROI. These values were then normalized to background levels measured in comparable areas of the same sample.

Tracheal branches were visualized either by their intrinsic autofluorescence using a 405 nm UV laser [15] or by the expression of membrane-bound GFP driven by a tracheal-specific Gal4 driver (UAS-mCD8GFP). Tracheal coverage was quantified as pixel area per muscle fiber from maximum intensity Z-projections acquired at 20× magnification. Quantification was performed using the “Skeletonize” plugin in ImageJ, based on the method described by Perochon et al. (2021) [18], with minor modifications. Briefly, maximum intensity projections were generated from each confocal stack, tracheal branches were segmented by thresholding, and the resulting images were skeletonized. Skeleton pixel intensity was then measured specifically within injured muscle fibers and their corresponding contralateral control fibers. For Figure 2E, square regions of interest (ROIs) were placed at the injury site, as well as in proximal and distal regions, to assess local tracheal enrichment. Hemocyte and dSRF-positive cell numbers were quantified manually using ImageJ.

Graphs and statistical analyses were performed using GraphPad Prism. Pair comparisons were statistically tested with a two-sided Student's t-test. NS, not significant ($p>0.05$); *$p < 0.05$, **$p < 0.01$, ***$p < 0.001$ ****$p< 0.0001$.

Acknowledgments

We would like to thank Jennifer Zanet, Cedric Polesello, Sougata Roy, Ruth Lehmann, Maurice Ringuette, Jean-Paul Vincent, and Mark A. Krasnow, as well as the Bloomington Drosophila Stock Center, the Vienna Drosophila Resource Center (VDRC), and the Developmental Studies Hybridoma Bank for providing *Drosophila* strains and antibodies. We are grateful to Juila Cordero, Lucas Waltzer, Laetitia Bataille, Alain Vincent, and Michèle Crozatier for their critical reading of the manuscript, and to other members of H.B's laboratory for valuable discussions. We also thank Emmanuel Gallaud for helpful input during the early phases of the project. We acknowledge Xavier Pinson from the Microscopy Rennes Imaging Center (MRic, BIOSIT, Biogenouest) for technical assistance, and Cyrille Surbled for fly stock maintenance and technical help. Work in the Boukhatmi lab was supported by an AFM-Téléthon Trampoline Grant (#23108), ATIP-Avenir (CNRS), and ANR GenepiMuSC (ANR-23-CE13-0006). N.A. was supported by an AFM-Téléthon PhD fellowship (#23846) and an FRM fellowship (FDT202404018608). Work in the Cordero lab was supported by a Sir Henry Dale Fellowship (Wellcome Trust and Royal Society, 104103/Z/14/Z), a Wellcome ISSF Returner Scheme (204820/Z/16/Z), and a Tenovus Fellowship (Tenovus/S22-28) to J.P.

Competing interest

The authors declare that they have no competing interests.

Reference

1. Sun F, Poss KD. Inter-organ communication during tissue regeneration. Development. 2023;150(23). Epub 20231127. doi: 10.1242/dev.202166. PubMed PMID: 38010139; PubMed Central PMCID: PMCPMC10730022.
2. Rodriguez C, Timoteo-Ferreira F, Minchiotti G, Brunelli S, Guardiola O. Cellular interactions and microenvironment dynamics in skeletal muscle regeneration and disease. Front Cell Dev Biol. 2024;12:1385399. Epub 20240522. doi: 10.3389/fcell.2024.1385399. PubMed PMID: 38840849; PubMed Central PMCID: PMCPMC11150574.

578 3. Koike H, Manabe I, Oishi Y. Mechanisms of cooperative cell-cell interactions in skeletal
579 muscle regeneration. Inflamm Regen. 2022;42(1):48. Epub 20221116. doi: 10.1186/s41232-
580 022-00234-6. PubMed PMID: 36380396; PubMed Central PMCID: PMCPMC9667595.
581 4. Ratnayake D, Nguyen PD, Rossello FJ, Wimmer VC, Tan JL, Galvis LA, et al.
582 Macrophages provide a transient muscle stem cell niche via NAMPT secretion. Nature.
583 2021;591(7849):281-7. Epub 20210210. doi: 10.1038/s41586-021-03199-7. PubMed PMID:
584 33568815.
585 5. Manneken JD, Currie PD. Macrophage-stem cell crosstalk: regulation of the stem cell
586 niche. Development. 2023;150(8). Epub 20230427. doi: 10.1242/dev.201510. PubMed PMID:
587 37102706.
588 6. Latroche C, Gitiaux C, Chretien F, Desguerre I, Mounier R, Chazaud B. Skeletal Muscle
589 Microvasculature: A Highly Dynamic Lifeline. Physiology (Bethesda). 2015;30(6):417-27. doi:
590 10.1152/physiol.00026.2015. PubMed PMID: 26525341.
591 7. Webster MT, Manor U, Lippincott-Schwartz J, Fan CM. Intravital Imaging Reveals
592 Ghost Fibers as Architectural Units Guiding Myogenic Progenitors during Regeneration. Cell
593 Stem Cell. 2016;18(2):243-52. Epub 20151210. doi: 10.1016/j.stem.2015.11.005. PubMed
594 PMID: 26686466; PubMed Central PMCID: PMCPMC4744135.
595 8. Droujinine IA, Perrimon N. Interorgan Communication Pathways in Physiology: Focus
596 on Drosophila. Annu Rev Genet. 2016;50:539-70. Epub 20161010. doi: 10.1146/annurev-
597 genet-121415-122024. PubMed PMID: 27732790; PubMed Central PMCID:
598 PMCPMC5506552.
599 9. Boukhatmi H, Bray S. A population of adult satellite-like cells in Drosophila is
600 maintained through a switch in RNA-isoforms. Elife. 2018;7. doi: 10.7554/eLife.35954.
601 PubMed PMID: 29629869; PubMed Central PMCID: PMCPMC5919756.
602 10. Chaturvedi D, Reichert H, Gunage RD, VijayRaghavan K. Identification and functional
603 characterization of muscle satellite cells in Drosophila. Elife. 2017;6. doi:
604 10.7554/eLife.30107. PubMed PMID: 29072161; PubMed Central PMCID: PMCPMC5681227.
605 11. Catalani E, Zecchini S, Giovarelli M, Cherubini A, Del Quondam S, Brunetti K, et al.
606 RACK1 is evolutionary conserved in satellite stem cell activation and adult skeletal muscle
607 regeneration. Cell Death Discovery. 2022;8(1):459. Epub 20221118. doi: 10.1038/s41420-
608 022-01250-8. PubMed PMID: 36396939; PubMed Central PMCID: PMCPMC9672362.
609 12. Jawkar S, Nongthomba U. Indirect flight muscles in Drosophila melanogaster as a
610 tractable model to study muscle development and disease. Int J Dev Biol. 2020;64(1-2-
611 3):167-73. doi: 10.1387/ijdb.190333un. PubMed PMID: 32659005.
612 13. Sanchez Bosch P, Makhijani K, Herboso L, Gold KS, Baginsky R, Woodcock KJ, et al.
613 Adult Drosophila Lack Hematopoiesis but Rely on a Blood Cell Reservoir at the Respiratory
614 Epithelia to Relay Infection Signals to Surrounding Tissues. Dev Cell. 2019;51(6):787-803 e5.
615 Epub 20191114. doi: 10.1016/j.devcel.2019.10.017. PubMed PMID: 31735669; PubMed
616 Central PMCID: PMCPMC7263735.
617 14. Peterson SJ, Krasnow MA. Subcellular trafficking of FGF controls tracheal invasion of
618 Drosophila flight muscle. Cell. 2015;160(1-2):313-23. Epub 2015/01/06. doi:
619 10.1016/j.cell.2014.11.043. PubMed PMID: 25557078; PubMed Central PMCID:
620 PMCPMC4577243.
621 15. Sauerwald J, Backer W, Matzat T, Schnorrer F, Luschnig S. Matrix metalloproteinase 1
622 modulates invasive behavior of tracheal branches during entry into Drosophila flight muscles.
623 Elife. 2019;8. Epub 2019/10/03. doi: 10.7554/eLife.48857. PubMed PMID: 31577228;
624 PubMed Central PMCID: PMCPMC6795481.

16. Hayashi S, Kondo T. Development and Function of the Drosophila Tracheal System. Genetics. 2018;209(2):367-80. doi: 10.1534/genetics.117.300167. PubMed PMID: 29844090; PubMed Central PMCID: PMCPMC5972413.
17. Affolter M, Shilo BZ. Genetic control of branching morphogenesis during Drosophila tracheal development. Curr Opin Cell Biol. 2000;12(6):731-5. doi: 10.1016/s0955-0674(00)00160-5. PubMed PMID: 11063940.
18. Perochon J, Yu Y, Aughey GN, Medina AB, Southall TD, Cordero JB. Dynamic adult tracheal plasticity drives stem cell adaptation to changes in intestinal homeostasis in Drosophila. Nat Cell Biol. 2021;23(5):485-96. Epub 2021/05/12. doi: 10.1038/s41556-021-00676-z. PubMed PMID: 33972729; PubMed Central PMCID: PMCPMC7610788.
19. Tamamouna V, Rahman MM, Petersson M, Charalambous I, Kux K, Mainor H, et al. Remodelling of oxygen-transporting tracheoles drives intestinal regeneration and tumorigenesis in Drosophila. Nat Cell Biol. 2021;23(5):497-510. Epub 20210510. doi: 10.1038/s41556-021-00674-1. PubMed PMID: 33972730; PubMed Central PMCID: PMCPMC8567841.
20. Medina AB, Perochon J, Tian Y, Johnson CT, Holcombe J, Ramesh P, et al. Neuroendocrine control of intestinal regeneration through the vascular niche in Drosophila. Dev Cell. 2025;60(22):3085-101 e6. Epub 20250721. doi: 10.1016/j.devcel.2025.06.036. PubMed PMID: 40695286.
21. Chu WC, Hayashi S. Mechano-chemical enforcement of tendon apical ECM into nano-filaments during Drosophila flight muscle development. Curr Biol. 2021;31(7):1366-78 e7. Epub 20210204. doi: 10.1016/j.cub.2021.01.010. PubMed PMID: 33545042.
22. Murphy MM, Lawson JA, Mathew SJ, Hutcheson DA, Kardon G. Satellite cells, connective tissue fibroblasts and their interactions are crucial for muscle regeneration. Development. 2011;138(17):3625-37. doi: 10.1242/dev.064162. PubMed PMID: 21828091; PubMed Central PMCID: PMCPMC3152921.
23. Orfanos Z, Sparrow JC. Myosin isoform switching during assembly of the Drosophila flight muscle thick filament lattice. J Cell Sci. 2013;126(Pt 1):139-48. Epub 20121123. doi: 10.1242/jcs.110361. PubMed PMID: 23178940.
24. Sarov M, Barz C, Jambor H, Hein MY, Schmied C, Suchold D, et al. A genome-wide resource for the analysis of protein localisation in Drosophila. Elife. 2016;5:e12068. Epub 20160220. doi: 10.7554/eLife.12068. PubMed PMID: 26896675; PubMed Central PMCID: PMCPMC4805545.
25. Varland S, Silva RD, Kjosas I, Faustino A, Bogaert A, Billmann M, et al. N-terminal acetylation shields proteins from degradation and promotes age-dependent motility and longevity. Nat Commun. 2023;14(1):6774. Epub 20231027. doi: 10.1038/s41467-023-42342-y. PubMed PMID: 37891180; PubMed Central PMCID: PMCPMC10611716.
26. Boulet M, Renaud Y, Lapraz F, Benmimoun B, Vandel L, Waltzer L. Characterization of the Drosophila Adult Hematopoietic System Reveals a Rare Cell Population With Differentiation and Proliferation Potential. Front Cell Dev Biol. 2021;9:739357. Epub 20211013. doi: 10.3389/fcell.2021.739357. PubMed PMID: 34722521; PubMed Central PMCID: PMCPMC8550105.
27. Wu WH, Kuo TH, Kao CW, Girardot C, Hung SJ, Liu T, et al. Expanding the mesodermal transcriptional network by genome-wide identification of Zinc finger homeodomain 1 (Zfh1) targets. FEBS Lett. 2019;593(14):1698-710. Epub 20190529. doi: 10.1002/1873-3468.13443. PubMed PMID: 31093969.

671 28. Ghabrial A, Luschnig S, Metzstein MM, Krasnow MA. Branching morphogenesis of the
672 Drosophila tracheal system. Annu Rev Cell Dev Biol. 2003;19:623-47. Epub 2003/10/23. doi:
673 10.1146/annurev.cellbio.19.031403.160043. PubMed PMID: 14570584.
674 29. Jarecki J, Johnson E, Krasnow MA. Oxygen regulation of airway branching in
675 Drosophila is mediated by branchless FGF. Cell. 1999;99(2):211-20. doi: 10.1016/s0092-
676 8674(00)81652-9. PubMed PMID: 10535739.
677 30. Zhao Y, Alexandre C, Kelly G, Perez-Mockus G, Vincent1 J-P. Growth-induced
678 physiological hypoxia correlates with growth deceleration during normal development.
679 bioRxiv. 2024. doi: https://doi.org/10.1101/2024.06.04.597345.
680 31. Du L, Sohr A, Yan G, Roy S. Feedback regulation of cytoneme-mediated transport
681 shapes a tissue-specific FGF morphogen gradient. Elife. 2018;7. Epub 20181017. doi:
682 10.7554/eLife.38137. PubMed PMID: 30328809; PubMed Central PMCID: PMCPMC6224196.
683 32. Wang X, Harris RE, Bayston LJ, Ashe HL. Type IV collagens regulate BMP signalling in
684 Drosophila. Nature. 2008;455(7209):72-7. doi: 10.1038/nature07214. PubMed PMID:
685 18701888.
686 33. Gold KS, Bruckner K. Macrophages and cellular immunity in Drosophila melanogaster.
687 Semin Immunol. 2015;27(6):357-68. Epub 20160423. doi: 10.1016/j.smim.2016.03.010.
688 PubMed PMID: 27117654; PubMed Central PMCID: PMCPMC5012540.
689 34. Bunt S, Hooley C, Hu N, Scahill C, Weavers H, Skaer H. Hemocyte-secreted type IV
690 collagen enhances BMP signaling to guide renal tubule morphogenesis in Drosophila. Dev
691 Cell. 2010;19(2):296-306. doi: 10.1016/j.devcel.2010.07.019. PubMed PMID: 20708591;
692 PubMed Central PMCID: PMCPMC2941037.
693 35. Bradshaw AD. The role of SPARC in extracellular matrix assembly. J Cell Commun
694 Signal. 2009;3(3-4):239-46. Epub 20091002. doi: 10.1007/s12079-009-0062-6. PubMed
695 PMID: 19798598; PubMed Central PMCID: PMCPMC2778582.
696 36. Chioran A, Duncan S, Catalano A, Brown TJ, Ringuette MJ. Collagen IV trafficking: The
697 inside-out and beyond story. Dev Biol. 2017;431(2):124-33. Epub 20171002. doi:
698 10.1016/j.ydbio.2017.09.037. PubMed PMID: 28982537.
699 37. Maddaluno L, Urwyler C, Werner S. Fibroblast growth factors: key players in
700 regeneration and tissue repair. Development. 2017;144(22):4047-60. doi:
701 10.1242/dev.152587. PubMed PMID: 29138288.
702 38. Osborn DPS, Li K, Cutty SJ, Nelson AC, Wardle FC, Hinits Y, et al. Fgf-driven Tbx protein
703 activities directly induce myf5 and myod to initiate zebrafish myogenesis. Development.
704 2020;147(8). Epub 20200428. doi: 10.1242/dev.184689. PubMed PMID: 32345657; PubMed
705 Central PMCID: PMCPMC7197714.
706 39. Floss T, Arnold HH, Braun T. A role for FGF-6 in skeletal muscle regeneration. Genes
707 Dev. 1997;11(16):2040-51. doi: 10.1101/gad.11.16.2040. PubMed PMID: 9284044; PubMed
708 Central PMCID: PMCPMC316448.
709 40. Lagha M, Kormish JD, Rocancourt D, Manceau M, Epstein JA, Zaret KS, et al. Pax3
710 regulation of FGF signaling affects the progression of embryonic progenitor cells into the
711 myogenic program. Genes Dev. 2008;22(13):1828-37. doi: 10.1101/gad.477908. PubMed
712 PMID: 18593883; PubMed Central PMCID: PMCPMC2492669.
713 41. Yablonka-Reuveni Z, Rivera AJ. Proliferative Dynamics and the Role of FGF2 During
714 Myogenesis of Rat Satellite Cells on Isolated Fibers. Basic Appl Myol. 1997;7(3-amp4):189-
715 202. PubMed PMID: 26052220; PubMed Central PMCID: PMCPMC4457462.
716 42. Zofkie W, Southard SM, Braun T, Lepper C. Fibroblast growth factor 6 regulates sizing
717 of the muscle stem cell pool. Stem Cell Reports. 2021;16(12):2913-27. Epub 20211104. doi:

718 10.1016/j.stemcr.2021.10.006. PubMed PMID: 34739848; PubMed Central PMCID:
719 PMCPMC8693628.
720 43. Sutherland D, Samakovlis C, Krasnow MA. branchless encodes a Drosophila FGF
721 homolog that controls tracheal cell migration and the pattern of branching. Cell.
722 1996;87(6):1091-101. doi: 10.1016/s0092-8674(00)81803-6. PubMed PMID: 8978613.
723 44. Zhang W, Liu Y, Zhang H. Extracellular matrix: an important regulator of cell functions
724 and skeletal muscle development. Cell Biosci. 2021;11(1):65. Epub 20210331. doi:
725 10.1186/s13578-021-00579-4. PubMed PMID: 33789727; PubMed Central PMCID:
726 PMCPMC8011170.
727 45. Molina T, Fabre P, Dumont NA. Fibro-adipogenic progenitors in skeletal muscle
728 homeostasis, regeneration and diseases. Open Biol. 2021;11(12):210110. Epub 20211208.
729 doi: 10.1098/rsob.210110. PubMed PMID: 34875199; PubMed Central PMCID:
730 PMCPMC8651418.
731 46. Mase A, Augsburger J, Bruckner K. Macrophages and Their Organ Locations Shape
732 Each Other in Development and Homeostasis - A Drosophila Perspective. Front Cell Dev Biol.
733 2021;9:630272. Epub 20210311. doi: 10.3389/fcell.2021.630272. PubMed PMID: 33777939;
734 PubMed Central PMCID: PMCPMC7991785.
735 47. Subasi BS, Grabe V, Kaltenpoth M, Rolff J, Armitage SAO. How frequently are insects
736 wounded in the wild? A case study using Drosophila melanogaster. R Soc Open Sci.
737 2024;11(6):240256. Epub 20240626. doi: 10.1098/rsos.240256. PubMed PMID: 39100166;
738 PubMed Central PMCID: PMCPMC11296199.
739 48. Chechenova M, McLendon L, Dallas B, Stratton H, Kiani K, Gerberich E, et al. Muscle
740 degeneration in aging Drosophila flies: the role of mechanical stress. Skelet Muscle.
741 2024;14(1):20. Epub 20240820. doi: 10.1186/s13395-024-00352-4. PubMed PMID:
742 39164781; PubMed Central PMCID: PMCPMC11334408.
743 49. Siles L, Ninfali C, Cortes M, Darling DS, Postigo A. ZEB1 protects skeletal muscle from
744 damage and is required for its regeneration. Nature Communications. 2019;10(1):1364. Epub
745 20190325. doi: 10.1038/s41467-019-08983-8. PubMed PMID: 30910999; PubMed Central
746 PMCID: PMCPMC6434033.
747 50. Kirkwood TB. Understanding the odd science of aging. Cell. 2005;120(4):437-47. doi:
748 10.1016/j.cell.2005.01.027. PubMed PMID: 15734677.
749 51. Rodrigues D, Renaud Y, VijayRaghavan K, Waltzer L, Inamdar MS. Differential
750 activation of JAK-STAT signaling reveals functional compartmentalization in Drosophila blood
751 progenitors. Elife. 2021;10. Epub 20210217. doi: 10.7554/eLife.61409. PubMed PMID:
752 33594977; PubMed Central PMCID: PMCPMC7920551.
753 52. Lin L. Clonal Analysis of Growth Behaviors During Drosophila Larval Tracheal
754 Development In Doctoral thesis: University of Basel; 2009.
755 53. Antonello ZA, Reiff T, Ballesta-Illan E, Dominguez M. Robust intestinal homeostasis
756 relies on cellular plasticity in enteroblasts mediated by miR-8-Escargot switch. EMBO J.
757 2015;34(15):2025-41. doi: 10.15252/embj.201591517. PubMed PMID: 26077448; PubMed
758 Central PMCID: PMCPMC4551350.
759 54. Leroux E, Ammar N, Moinet S, Pecot T, Boukhatmi H. Studying Muscle Transcriptional
760 Dynamics at Single-molecule Scales in Drosophila. J Vis Exp. 2023;(199). Epub 20230908. doi:
761 10.3791/65713. PubMed PMID: 37747217.
762 55. Chakraborty K, VijayRaghavan K, Gunage R. A Method to Injure, Dissect and Image
763 Indirect Flight Muscle of Drosophila. Bio Protoc. 2018;8(10):e2860. Epub 20180520. doi:

764 10.21769/BioProtoc.2860. PubMed PMID: 34285976; PubMed Central PMCID:
765 PMCPMC8275216.
766
767

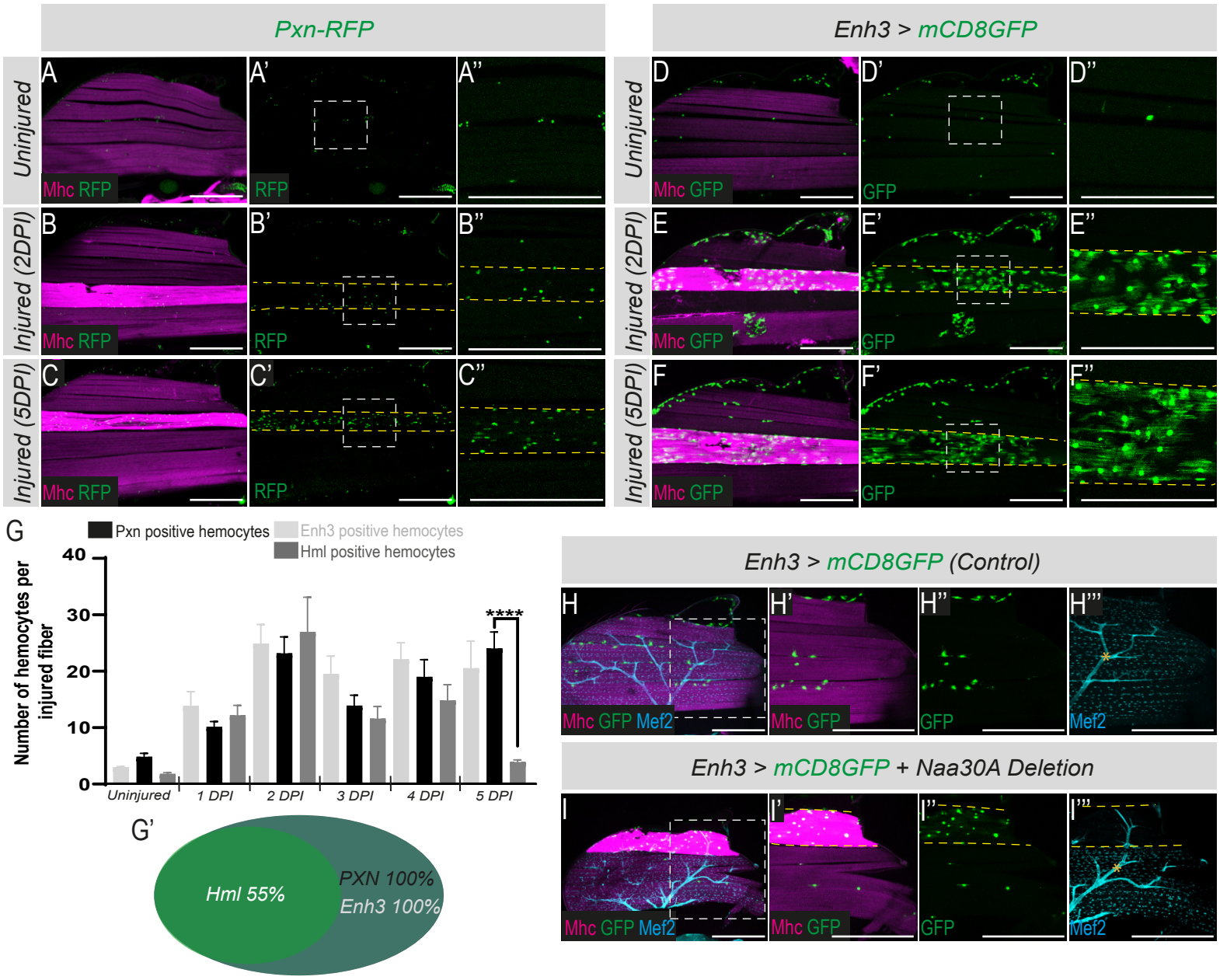
Pxn-RFP
Enh3 > mCD8GFP
Uninjured
Injured (2DPI)
Injured (5DPI)
A
A'
A''
B
B'
B''
C
C'
C''
D
D'
D''
E
E'
E''
F
F'
F''
Mhc RFP
RFP
Mhc GFP
GFP
G
Pxn positive hemocytes
Enh3 positive hemocytes
Hml positive hemocytes
Number of hemocytes per injured fiber
40
30
20
10
0
****
Uninjured
1 DPI
2 DPI
3 DPI
4 DPI
5 DPI
G'
Hml 55%
PXN 100%
Enh3 100%
Enh3 > mCD8GFP (Control)
H
H'
H''
H'''
Mhc GFP Mef2
Mhc GFP
GFP
Mef2
Enh3 > mCD8GFP + Naa30A Deletion
I
I'
I''
I'''
Mhc GFP Mef2
Mhc GFP
GFP
Mef2

Figure 1

Figure 1. Hemocytes are specifically recruited to the damaged muscle fiber. (A-F). Adult indirect flight muscles (IFMs) imaged under uninjured conditions and at 2-and 5-days post-injury (2DPI and 5DPI). Mhc (magenta) marks muscles. Hemocytes (green) are visualized using the following reporters: *Pxn-RFP* in (A-C'') and *Enh3-Gal4; UAS-mCD8GFP* in (D-F''). Dashed yellow outlines indicate injured muscle fibers showing elevated Mhc expression. Boxed regions are magnified 5X. **(G).** Time-course analysis of hemocytes recruitment at 1, 2, 3, 4 and 5 DPI reveals heterogeneous kinetics of response to muscle damage. Enh3-positive, Pxn-positive, and Hml-positive hemocytes are represented by light gray, black, and dark gray bars, respectively (****$p < 0.0001$, Student's t-test; $n \geq 10$ heminota per condition). **(G').** Schematic representation of the proportion of recruited hemocytes expressing different reporters. **(H-I''').** Distribution of hemocytes visualized with *Enh3-Gal4; UAS-mCD8GFP* (green) in control muscles (H-H''') and *Naa30A* mutants (I-I'''). Muscles and muscle nuclei are stained with Mhc (magenta) and Mef2 (cyan) respectively. Scale bars: 200µm. Asterisks in panels H''' and I''' mark non-specific signal detected in motoneurons.

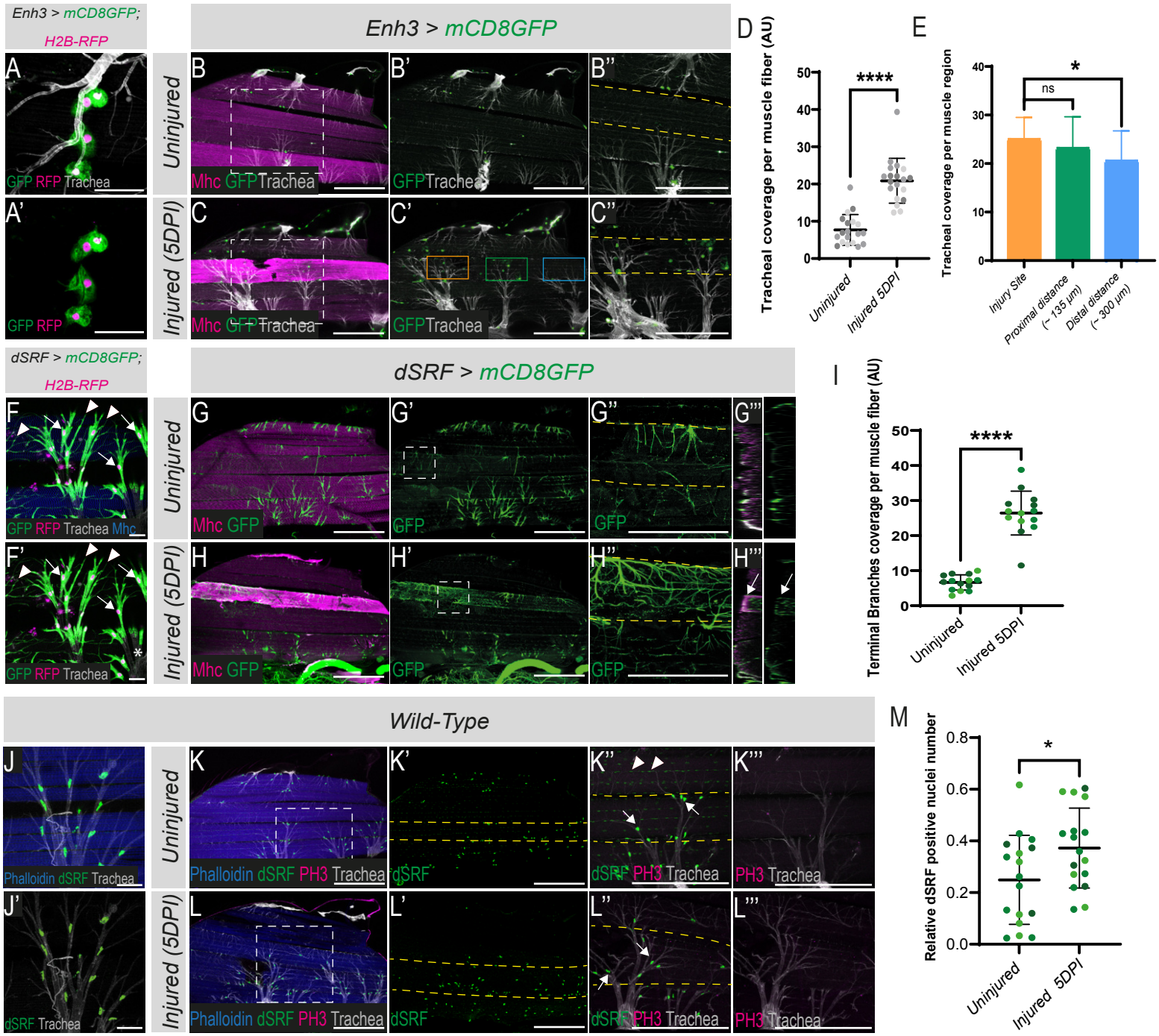
Enh3 > mCD8GFP;
H2B-RFP
Enh3 > mCD8GFP
Uninjured
Injured (5DPI)
GFP RFP Trachea
Mhc GFP Trachea
GFP Trachea
GFP RFP
D
Tracheal coverage per muscle fiber (AU)
****
Uninjured
Injured 5DPI
E
Tracheal coverage per muscle region
*
ns
Injury Site
Proximal distance (~ 135 µm)
Distal distance (~ 300 µm)
dSRF > mCD8GFP;
H2B-RFP
dSRF > mCD8GFP
GFP RFP Trachea Mhc
Mhc GFP
GFP
I
Terminal Branches coverage per muscle fiber (AU)
****
Uninjured
Injured 5DPI
Wild-Type
Phalloidin dSRF Trachea
Phalloidin dSRF PH3 Trachea
dSRF
dSRF PH3 Trachea
PH3 Trachea
dSRF Trachea
M
Relative dSRF positive nuclei number
*
Uninjured
Injured 5DPI

Figure 2

Figure 2. Muscle damage induces directed tracheal remodelling. (A-A'). Hemocytes (green/magenta; *Enh3-Gal4, UAS-mCD8GFP; UAS-H2B-RFP*) are associated to the muscle tracheal cells (gray, autofluorescence). Scale bars: 25 µm. **(B-C'').** Distribution of tracheal branches (gray, autofluorescence) and hemocytes (green, *Enh3-Gal4; UAS-mCD8GFP*) in uninjured IFMs (B-B'') and at 5DPI (C-C''). Muscles are labeled with Mhc (magenta). (B'', C''). Boxed regions from (B and C), magnified 2X. Scale bars: 200 µm. **(D).** Quantification of tracheal coverage in (B) and (C) (****$p < 0.0001$, Student's t-test; n = 19 heminota per condition; light, dark, and intermediate shading indicate data points from three independent replicates). **(E).** Quantification of tracheal coverage in (C) at the injury site (orange box), adjacent to the injury site (green box, approximately 135 µm away from the injury site), and at distant regions (blue box, within 300 µm of the lesion border) (*$p= 0.0142$, Student's t-test; n=19 heminota). **(F-F').** dSRF-Gal4 marks muscle-associated terminal tracheal cells (TTCs). TTC membranes (green) and nuclei (magenta) are indicated by arrowheads and arrows, respectively (*dSRF-Gal4, UAS-mCD8GFP; UAS-H2B-RFP*). dSRF-Gal4 is inactive in primary tracheal branches (asterisks in F'). Muscles are labeled with Mhc (blue). Scale bars: 25 µm. **(G-H''').** TTCs distribution in IFMs (green, *dSRF-Gal4, UAS-mCD8GFP*) in uninjured muscles (G-G''') and at 5DPI (H-H'''). Muscles are labeled with Mhc (magenta). (G'', H''). 4.5X magnifications of boxed regions in (G') and (H'). Scale bar: 200 µm. (G''', H'''). Orthogonal views of (G'') and (H''). Arrow in (H''') indicates TTC enrichment at the injured muscle. **(I).** Quantification of TTCs coverage from (G) and (H) (****$p < 0.0001$, Student's t-test; n = 14 heminota per condition; light, dark, and intermediate shading points represent data points from three independent replicates). **(J-J').** dSRF (green) marks TTCs nuclei associated with IFMs. Scale bars: 25 µm. **(K-L''').** Distribution of TTCs nuclei (green) in IFMs under uninjured conditions (K-K''') and at 5DPI (L-L'''). Muscles are labeled with phalloidin (blue); tracheae are visualized by autofluorescence (gray). Anti-PH3 (magenta) is used to assess cell division. (K'', L''). 2X magnification of boxed regions in (K) and (L). Scale bars: 200 µm. Arrowheads and arrows indicate dSRF expression in the muscle and TTCs nuclei, respectively. **(M).** Proportion of TTCs nuclei located within a selected muscle relative to the total number of TTCs nuclei in the imaged sample (*$p = 0.036$, Student's t-test; n = 17 heminota per condition; light, dark, and intermediate shading indicate data points from three independent replicates).

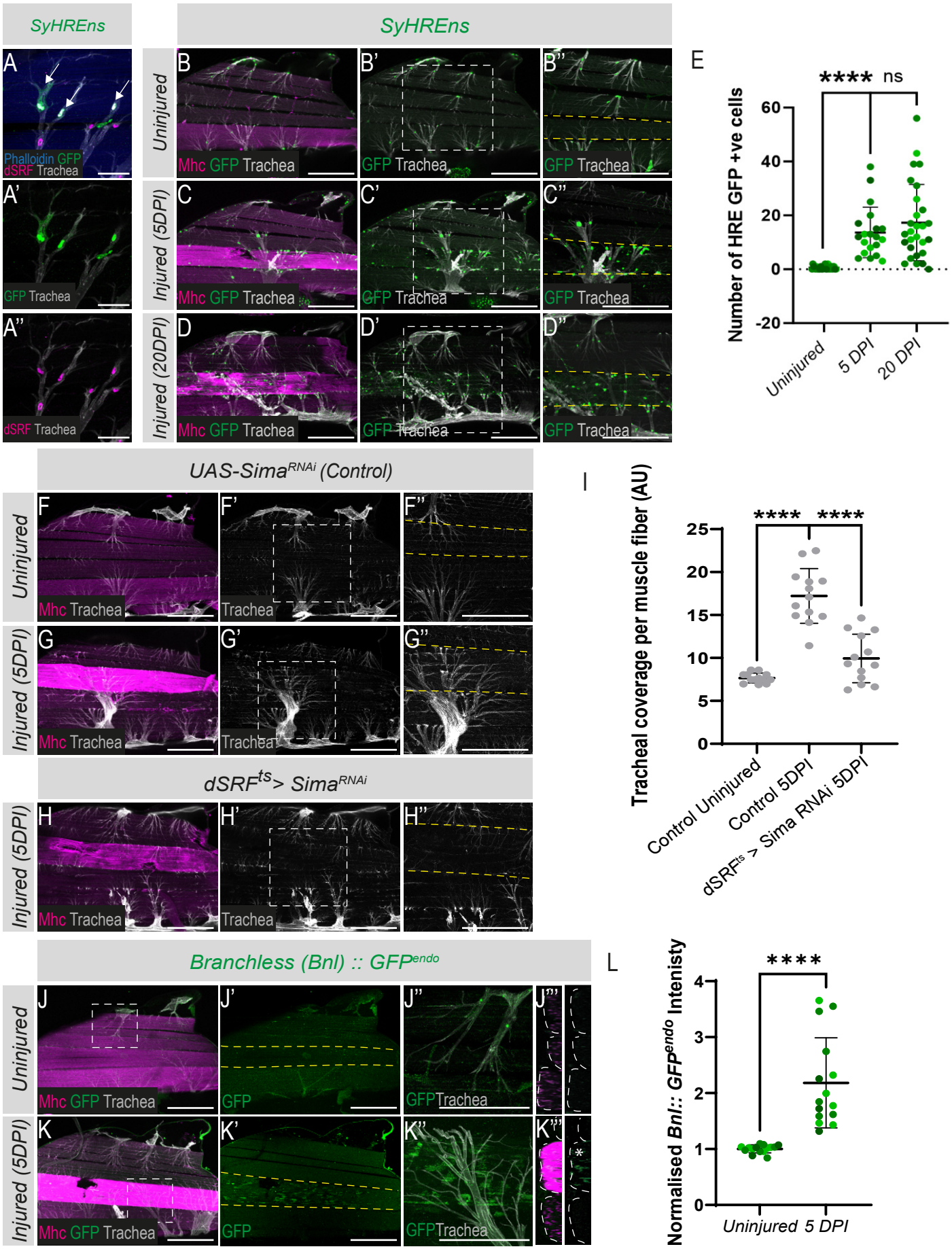
SyHREns
SyHREns
A
Phalloidin GFP
dSRF Trachea
A'
GFP Trachea
A''
dSRF Trachea
Uninjured
Injured (5DPI)
Injured (20DPI)
B
B'
B''
C
C'
C''
D
D'
D''
Mhc GFP Trachea
GFP Trachea
E
**** ns
Number of HRE GFP +ve cells
60
40
20
0
-20
Uninjured
5 DPI
20 DPI
UAS-Sima^RNAi (Control)
F
F'
F''
G
G'
G''
Mhc Trachea
Trachea
dSRF^ts> Sima^RNAi
H
H'
H''
I
Tracheal coverage per muscle fiber (AU)
**** ****
25
20
15
10
5
0
Control Uninjured
Control 5DPI
dSRF^ts > Sima RNAi 5DPI
Branchless (Bnl) :: GFP^endo
J
J'
J''
J'''
K
K'
K''
K'''
Mhc GFP Trachea
GFP
GFP Trachea
L
Normalised Bnl:: GFP^endo Intenisty
****
4
3
2
1
0
Uninjured
5 DPI

Figure 3

Figure 3. Local hypoxia in response to muscle damage drives tracheal branching. (A-A''). *SyHREns* reporter activity (green) is detected in a subset of TTCs marked by dSRF (magenta, arrows). Scale bars: 25 µm. **(B-D'').** Expression of the *SyHREns* reporter (green) in unijured IFMs (B-B''), at 5DPI (C-C'') and 20DPI (D-D''). Muscles are labeled with Mhc (magenta), and tracheal branches are visualized via autofluorescence (gray). (B'', C'' and D''). 2X magnification of the boxed regions in B', C' and D'. Scale bars: 200 µm. **(E).** Quantification of SyHREns positive cells (green) per injured muscle fiber (****$p < 0.0001$, Student's t-test; $n > 20$ heminota per condition; light, dark and intermediate shading indicate data points from three independent replicates). **(F-H'').** Sima (HIF-1α) downregulation in TTCs (*dSRF-Gal4; UAS-Sima^{RNAi}*) prevents tracheal recruitment at the injured fiber. (F'', G'' and H''). 2X magnification of the boxed regions in E', F' and G'. Scale bars: 200 µm. **(I).** Quantification of trachea coverage (****$p < 0.0001$, Student's t-test; $n = 13$ heminota per condition). **(J-K'').** Detection of Bnl (green, *Bnl::GFP^{endo}*) in control IFMs (J-J'') and at 5DPI (K-K''). Muscles are labeled with Mhc (magenta), and tracheal cells are visualized via autofluorescence (gray). (J'', K''). 4.5X magnification of the boxed regions in J and K. Scale bars: 200 µm. (J''', K'''). Orthogonal views of (J) and (K). Asterisk in K''' indicates Bnl::GFP^{endo} enrichment at the injured muscle. **(L).** Quantification of normalized Bnl::GFP^{endo} intensity level in uninjured and injured muscle fiber at 5DPI (***$p<0.0001$, Student t-test, $n = 15$ heminota per condition from three independent replicates).

hs-Flp; SME-FRT-STOP-FRT-Gal4 ; UAS-Bnl::GFP, tubGal80^{ts}

Without Heat Shock | 2 hours Heat Shock + 1 Day at 30°C | 2 hours Heat Shock + 5 Days at 30°C

A, A', B, B', C, C'

dSRF GFP Trachea

Branchless (Bnl)-LacZ

Bnl :: GFP^{endo} , Pxn-RFP

Uninjured

Injured (5DPI)

D, D', D''

Mhc βGal DAPI

βGal

E, E', E''

F, F', F''

Mhc GFP RFP Trachea

GFP RFP

G, G', G''

Enh3 > mCD8GFP (Control)

H, H', H''

PhalloidinGFP Trachea

Trachea

I, I', I''

Enh3 > mCD8GFP ; Bnl^{RNAi}

J, J', J''

K

Tracheal coverage per muscle fiber (AU)

30

20

10

0

****

****

ns

Control Uninjured

Control 5DPI

Enh3> Bnl^{RNAi} Uninjured

Enh3> Bnl^{RNAi} 5DPI

Flight assay

L

Section

Top

Middle

Bottom

Flight capacity

L'

***

*

Distribution of flies across tube sections (%)

90%

60%

30%

0%

Enh3-Gal4 Uninjured

Enh3-Gal4 5 DPI

Enh3^{ts}> Bnl^{RNAi} 5 DPI

M

Hemocytes recrutement

Bnl production

Tracheal remodelling

Maintain flight performance

Figure 4

Figure 4. Hemocytes deliver Bnl to injured muscle to promote tracheal recruitment. (A-C'). Local overexpression of UAS-Bnl::GFP (green) in adult IFMs using *SME-Gal4* driver induces enrichment of terminal tracheal cells (TTCs; dSRF, magenta) and increases tracheal branching (gray), compared with controls (A). Scale bars: 200 µm. **(D-E'').** *Bnl-LacZ* reporter expression (green) is downregulated specifically in of the injured muscle fibers overexpressing Mhc (magenta), the nuclei are marked with DAPI (blue). (D', E''). 3X magnification of the boxed regions in D and E. Scale bars: 200 µm. **(F-G'').** Endogenous Bnl expression (green, *Bnl::GFP*^{endo}) in uninjured IFMs (F-F'') and at 5DPI (G-G''). Muscles are labeled with Mhc (blue), tracheal branches are visualized via autofluorescence (gray), and hemocytes detected with the *Pxn-RFP* reporter (magenta). Arrows in G'' indicate Bnl localization around hemocytes recruited to the injured muscle. Scale bars: 200 µm. **(H-J'').** Downregulating *bnl* in the hemocytes (green, *Enh3-Gal4; UAS-mCD8GFP, UAS-Bnl*^{RNAi}) do not alter hemocytes recruitment but decreases tracheal invasion to the damaged fiber as shown in (J'-J'') and quantified in **(K)** (**** $p < 0.0001$, Student t-test; n = 16 heminota from two independent replicates). Scale bars: 200 µm. **(L).** Schematic representation of the flight-assay setup used to assess flight performance. Flies are released at the top of a graduated cylinder, and landing position across three vertical zones is recorded. **(L').** Quantification of the proportion of flies distributed across three sections under three conditions: *Control Uninjured*, *Control Injured (5DPI)* and *Enh3-Gal4; UAS-Bnl*^{RNAi} *Injured (5DPI)*. Bars indicate the percentage of flies landing in each of the three flight-assay zones (***$p<0.001$, * $p < 0.05$ Chi-2 test). **(M).** Schematic model of hemocyte-driven tracheal recruitment required to maintain flight capacity following muscle injury.

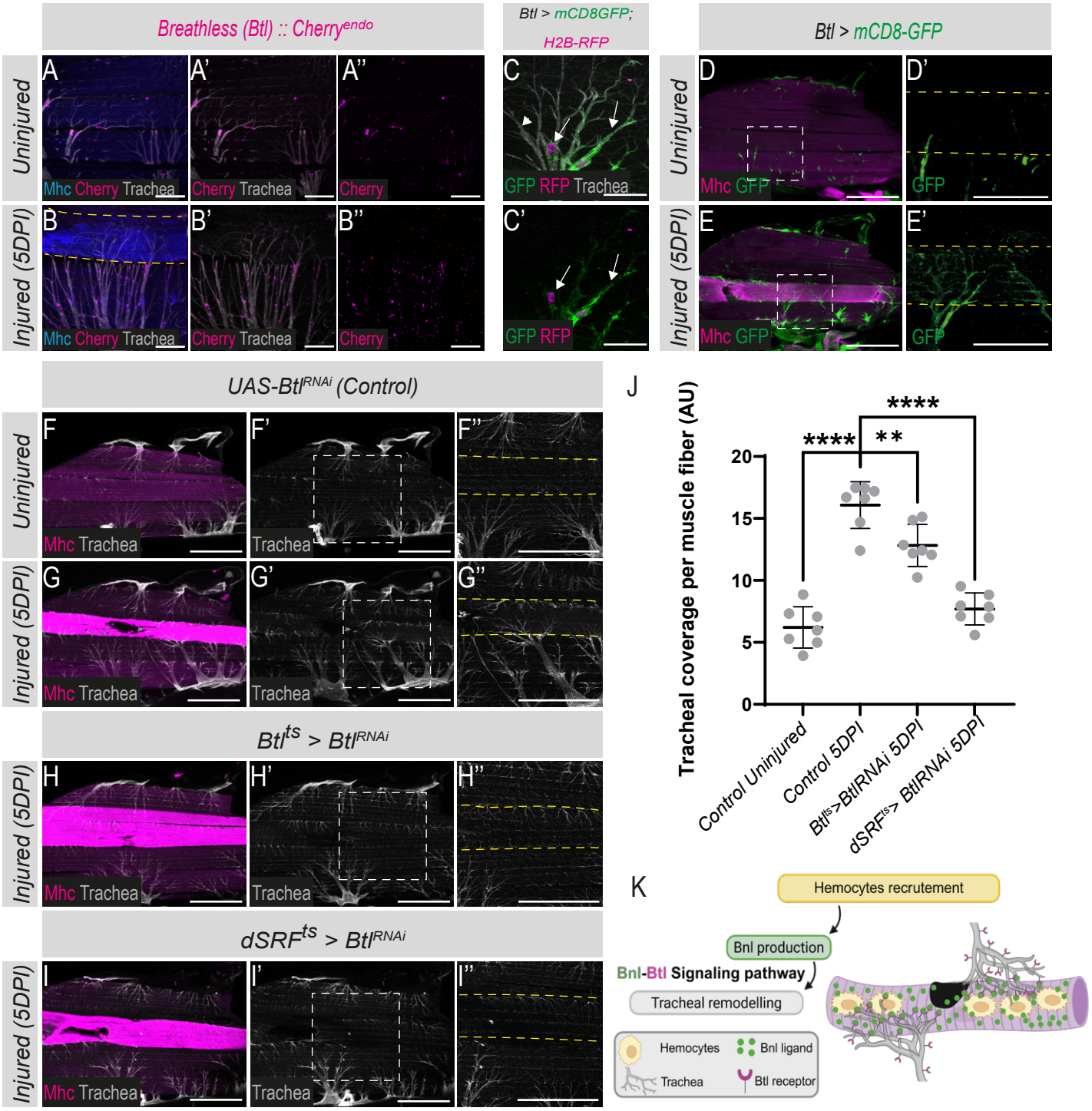
Breathless (Btl) :: Cherry^endo
Btl > mCD8GFP; H2B-RFP
Btl > mCD8-GFP
Uninjured
Injured (5DPI)
A
A'
A''
B
B'
B''
C
C'
D
D'
E
E'
Mhc Cherry Trachea
Cherry Trachea
Cherry
GFP RFP Trachea
GFP RFP
Mhc GFP
GFP
UAS-Btl^RNAi (Control)
Btl^ts > Btl^RNAi
dSRF^ts > Btl^RNAi
F
F'
F''
G
G'
G''
H
H'
H''
I
I'
I''
Mhc Trachea
Trachea
J
Tracheal coverage per muscle fiber (AU)
0
5
10
15
20
****
**
****
Control Uninjured
Control 5DPI
Btl^ts>BtlRNAi 5DPI
dSRF^ts> BtlRNAi 5DPI
K
Hemocytes recrutement
Bnl production
Bnl-Btl Signaling pathway
Tracheal remodelling
Hemocytes
Bnl ligand
Trachea
Btl receptor

Figure 5

Figure 5. The FGF receptor Breathless (Btl) is expressed along tracheal branches and is required for tracheal recruitment to the damaged muscle. (A-B''). Btl::Cherry^{endo} (magenta) is detected along tracheal branches (gray) associated with indirect flight muscles (IFMs) labelled with Mhc (blue), in either uninjured (A) or injured muscles (B). Scale bars: 50 µm. Dashed yellow outlines indicate injured muscle fibers showing elevated Mhc expression. **(C-C').** The *Btl-Gal4* driver (green and magenta; *Btl-Gal4, UAS-mCD8GFP; UASH2B-RFP*) is active in a subset of tracheal branches (arrows, C-C'). Arrowheads in C indicate the tracheal branches that do not express the *Btl-Gal4* driver. Scale bars: 25 µm. **(D-E').** Activity of the *Btl-Gal4* driver (green, *Btl-Gal4, UAS-mCD8GFP*) in uninjured condition (D-D') and at 5DPI (E-E'). Muscles are labelled with Mhc (magenta). Scale bars: 200 µm. **(F-I'').** Downregulating *btl* in the tracheal cells with either *Btl-Gal4* driver (*Btl-Gal4; UAS-Btl^{RNAi}*, H-H'') or *dSRF-Gal4* driver (*dSRF-Gal4, UAS- Btl^{RNAi}*, I-I'') prevents tracheal invasion to the damaged fiber. **(J).** Quantification of trachea coverage (****p <0.0001, **p=0.0053, Student's t-test; n = 7 heminota per condition). Scale bars: 200 µm. **(K).** Schematic model of hemocyte-driven Bnl activates tracheal cells recruitment via Bnl/Btl signalling pathway.

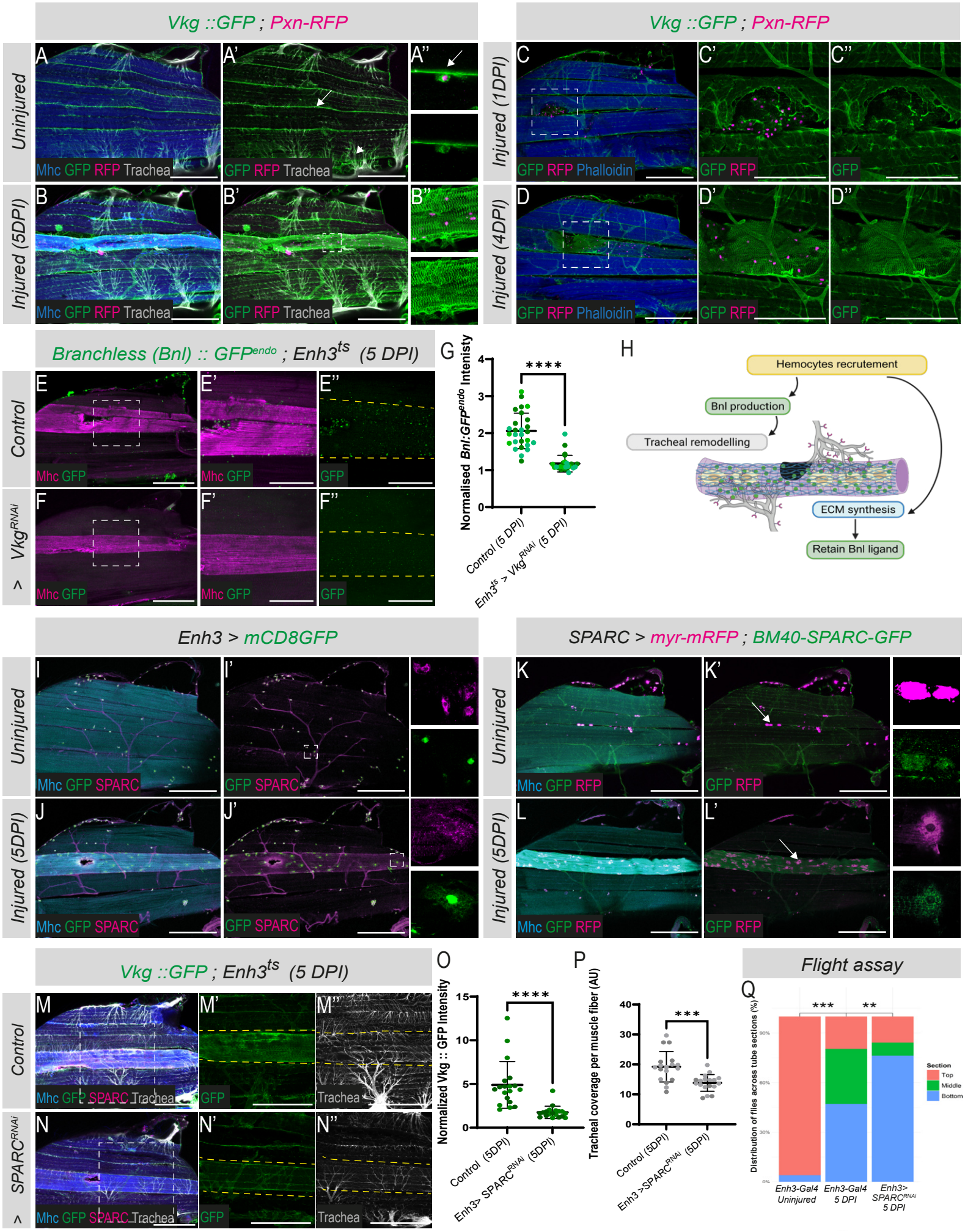
Vkg ::GFP ; Pxn-RFP
Uninjured
Injured (5DPI)
Mhc GFP RFP Trachea
GFP RFP Trachea
Vkg ::GFP ; Pxn-RFP
Injured (1DPI)
Injured (4DPI)
GFP RFP Phalloidin
GFP RFP
GFP
Branchless (Bnl) :: GFPendo ; Enh3ts (5 DPI)
Control
Vkg RNAi >
Mhc GFP
GFP
Normalised Bnl:GFPendo Intensity
****
Control (5 DPI)
Enh3ts > VkgRNAi (5 DPI)
Hemocytes recrutement
Bnl production
Tracheal remodelling
ECM synthesis
Retain Bnl ligand
Enh3 > mCD8GFP
Mhc GFP SPARC
GFP SPARC
SPARC > myr-mRFP ; BM40-SPARC-GFP
Mhc GFP RFP
GFP RFP
Vkg ::GFP ; Enh3ts (5 DPI)
SPARC RNAi >
Trachea
Normalized Vkg :: GFP Intensity
Control (5DPI)
Enh3> SPARCRNAi (5DPI)
Tracheal coverage per muscle fiber (AU)
***
Flight assay
Distribution of flies across tube sections (%)
**
Section
Top
Middle
Bottom
Enh3-Gal4 Uninjured
Enh3-Gal4 5 DPI
Enh3> SPARCRNAi 5 DPI

Figure 6

Figure 6. Hemocytes deposit ECM components at injury muscles to constrain Bnl to damaged muscle fibers and maintain muscle function. (A-A''). Collagen IV (green, *Vkg::GFP*) is detected at basal levels around muscle fibers (arrow, A'), tracheal branches (arrowheads, A'), and hemocytes (magenta, *Pxn-RFP*; arrow, A'') in uninjured conditions. **(B-B'').** At 5DPI, Collagen IV is strongly enriched on the injured muscle fibers, labelled with Mhc (blue). **(C-D'').** Hemocytes recruitment (magenta, *Pxn-RFP*) coincides with Collagen IV (green, *Vkg::GFP*) distribution on the injured muscle, at 1DPI and 4DPI. Muscles are labeled with phalloidin (blue). Scale bars: 200 µm. **(E-F'').** The endogenous Bnl (green, *Bnl::GFP*^{endo}) is enriched along damaged muscle fibers (magenta, Mhc) and is markedly reduced upon hemocyte-specific depletion of Collagen IV (*Enh3-Gal4, UAS-Vkg*^{RNAi}). **(G).** Quantification of normalized Bnl::GFP^{endo} intensity in injured fibers (****p<0.0001, Student t-test, n >27 heminota per condition from three independent replicates). **(H).** Schematic model of hemocyte-mediated ECM delivery required to confine Bnl to injured muscle fibers. **(I-I').** SPARC (magenta) is detected in the IFMs associated hemocytes visualized by *Enh3-Gal4* driver (green, *Enh3-Gal4, UAS-mCD8GFP*). **(J-J').** SPARC expression is increased in injured fibers compared to uninjured condition (I-I'). **(K-K').** Adult hemocytes (magenta; *SPARC-Gal4, UAS-myr-RFP*) express BM40-SPARC-GFP (green). **(L-L').** BM40-SPARC-GFP produced by adult hemocytes is broadly distributed along the injured muscle fibers. **(M-N').** Downregulation of *SPARC* in adult hemocytes (*Enh3-Gal4 > UAS-SPARC*^{RNAi}) reduces Collagen IV enrichment (green, *Vkg::GFP*) and impairs tracheal recruitment in injured fiber (gray, autofluorescence), as quantified in panels **(O)** and **(P)** respectively (O. ****p<0.0001, Student t-test, n = 20 heminota per condition from two independent replicates, P. ***p<0.001, Student t-test, n = 18 heminota per condition from two independent replicates). **(Q).** Quantification of the proportion of flies distributed across three sections (Top, Middle and Bottom) under three conditions: Control Uninjured, Control Injured (5DPI) and Enh3-Gal4; UAS-SPARC^{RNAi} Injured (5DPI) (***p<0.001, ** p < 0.01 Chi-2 test).

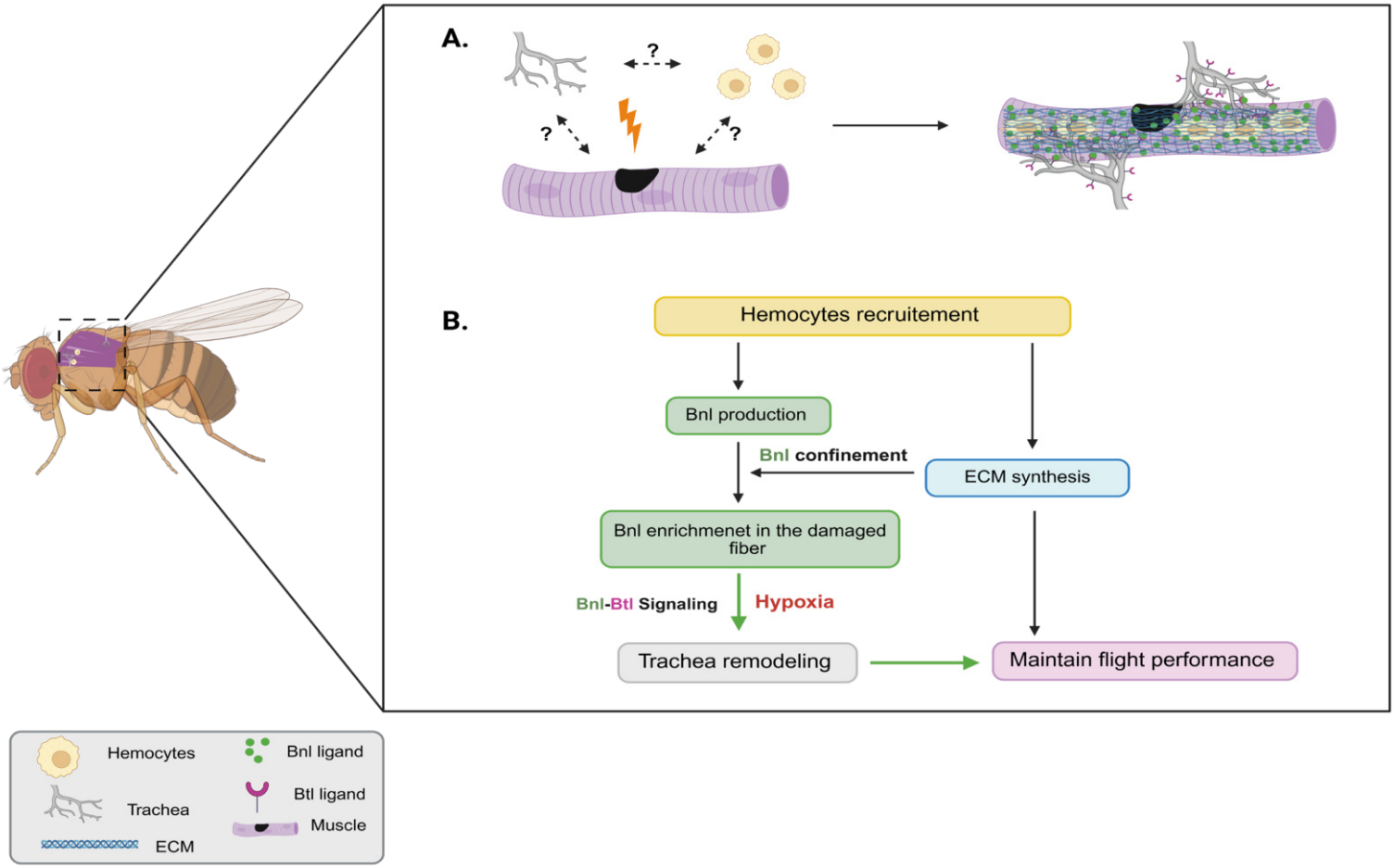
A.
?
?
?
B.
Hemocytes recruitement
Bnl production
Bnl confinement
ECM synthesis
Bnl enrichmenet in the damaged fiber
Bnl-Btl Signaling
Hypoxia
Trachea remodeling
Maintain flight performance
Hemocytes
Bnl ligand
Btl ligand
Trachea
Muscle
ECM

Figure 7

Figure 7. Hemocyte-muscle-tracheal intercellular signaling orchestrates tracheal remodelling and muscle repair after injury. (A). Schematic representation of the hemocyte-muscle-tracheal signaling module activated in response to muscle injury. **(B).** Upon muscle damage, hemocytes are rapidly recruited to the injured fiber, where they secrete the FGF-like ligand Branchless (Bnl), which activates its receptor Breathless (Btl) on tracheal cells. Bnl-Btl signaling drives tracheal remodeling and directional outgrowth toward the injured muscle. In parallel, hemocytes deposit extracellular matrix (ECM) components that retain Bnl and stabilize trachea-muscle attachments. Together, these coordinated cellular mechanisms promote muscle repair and preserve flight performance.

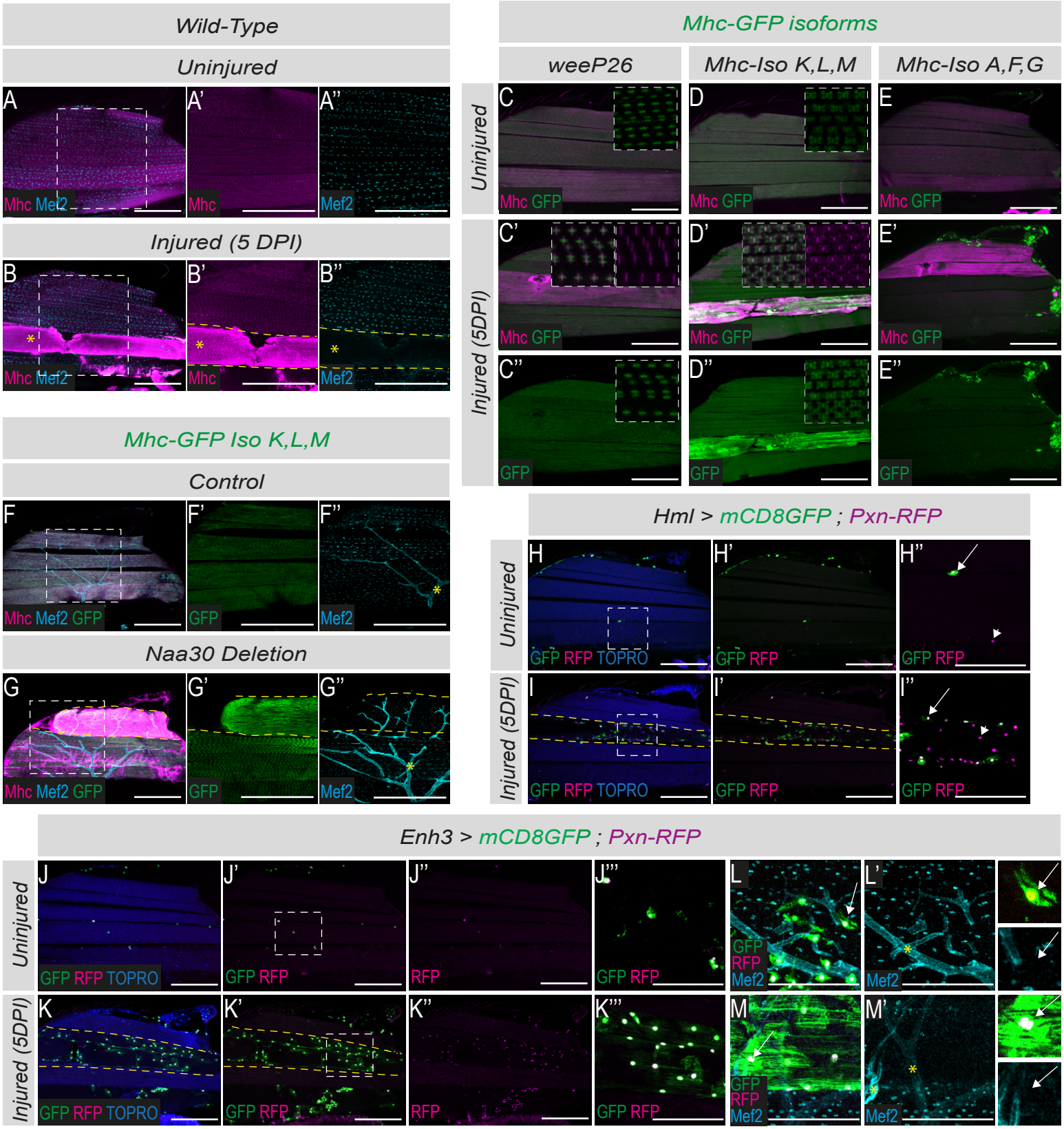
Wild-Type
Uninjured
A
A'
A''
Mhc Mef2
Mhc
Mef2
Injured (5 DPI)
B
B'
B''
Mhc Mef2
Mhc
Mef2
Mhc-GFP Iso K,L,M
Control
F
F'
F''
Mhc Mef2 GFP
GFP
Mef2
Naa30 Deletion
G
G'
G''
Mhc Mef2 GFP
GFP
Mef2
Mhc-GFP isoforms
weeP26
Mhc-Iso K,L,M
Mhc-Iso A,F,G
Uninjured
Injured (5DPI)
C
D
E
Mhc GFP
C'
D'
E'
Mhc GFP
C''
D''
E''
GFP
Hml > mCD8GFP ; Pxn-RFP
Uninjured
Injured (5DPI)
H
H'
H''
GFP RFP TOPRO
GFP RFP
I
I'
I''
GFP RFP TOPRO
GFP RFP
Enh3 > mCD8GFP ; Pxn-RFP
Uninjured
Injured (5DPI)
J
J'
J''
J'''
GFP RFP TOPRO
GFP RFP
RFP
L
L'
GFP
RFP
Mef2
K
K'
K''
K'''
M
M'

Figure S1

Figure S1. Mhc upregulation marks the damaged muscle fiber. (A-B''). IFMs stained for Mhc (magenta) and Mef2 (cyan) show upregulation of Mhc and downregulation of Mef2 in the injured fiber (asterisks, B'-B'') at 5DPI, compared to the uninjured IFMs (A'-A''). (A', B'). 2X magnification of the boxed regions in A and B. Scale bars: 200 µm. **(C-C'').** Expression of the embryonic Mhc isoform (*weeP26*, green) in uninjured (C) and injured (C'-C'') IFMs. Injury does not alter weeP26 expression (C' - C''). **(D-D'').** The shorter Mhc isoforms (*Mhc-Iso-K, L, M (fTRG500)*; green) colocalize with anti-Mhc staining (magenta) and are upregulated in injured muscle (D'-D''). **(E-E'').** The longer Mhc-GFP isoforms (*Mhc-Iso-A, F, G (fTRG519)*; green) are not expressed in adult IFMs and are not upregulated in response to muscle injury (E'-E''). Scale bars: 200 µm. **(F-G'').** In *Naa30A mutant* IFMs, defective muscle attachment correlates with increased Mhc expression (magenta, G), upregulation of short Mhc-GFP isoforms (green, G'), and a loss of Mef2 (cyan, G''). **(H-I'').** Co-expression of hemocytes markers *HmlΔ-Gal4, UAS-mCD8GFP* (green) and *Pxn-RFP* (magenta) reveals two subsets of hemocytes associated with the IFMs: Pxn+Hml+ (arrows) and Pxn+Hml- (arrowheads). Nuclei are visualized with TO-PRO (blue). Scale bars: 200 µm. (H''-I''). 3X magnification of the boxed regions in H and I. Scale bars: 100 µm. **(J-M').** Co-expression analysis of *Enh3-Gal4; UAS-mcD8GFP* (green) and *Pxn-RFP* (magenta) shows that all Enh3+ cells express Pxn (J'-K'). No Mef2 expression (cyan) is observed in these cells, in either undamaged (L') or damaged (M', dashed lines) fibers. Scale bars: 200 µm. Yellow asterisks in panels F', G'' and L' mark non-specific signal detected in motoneurons.

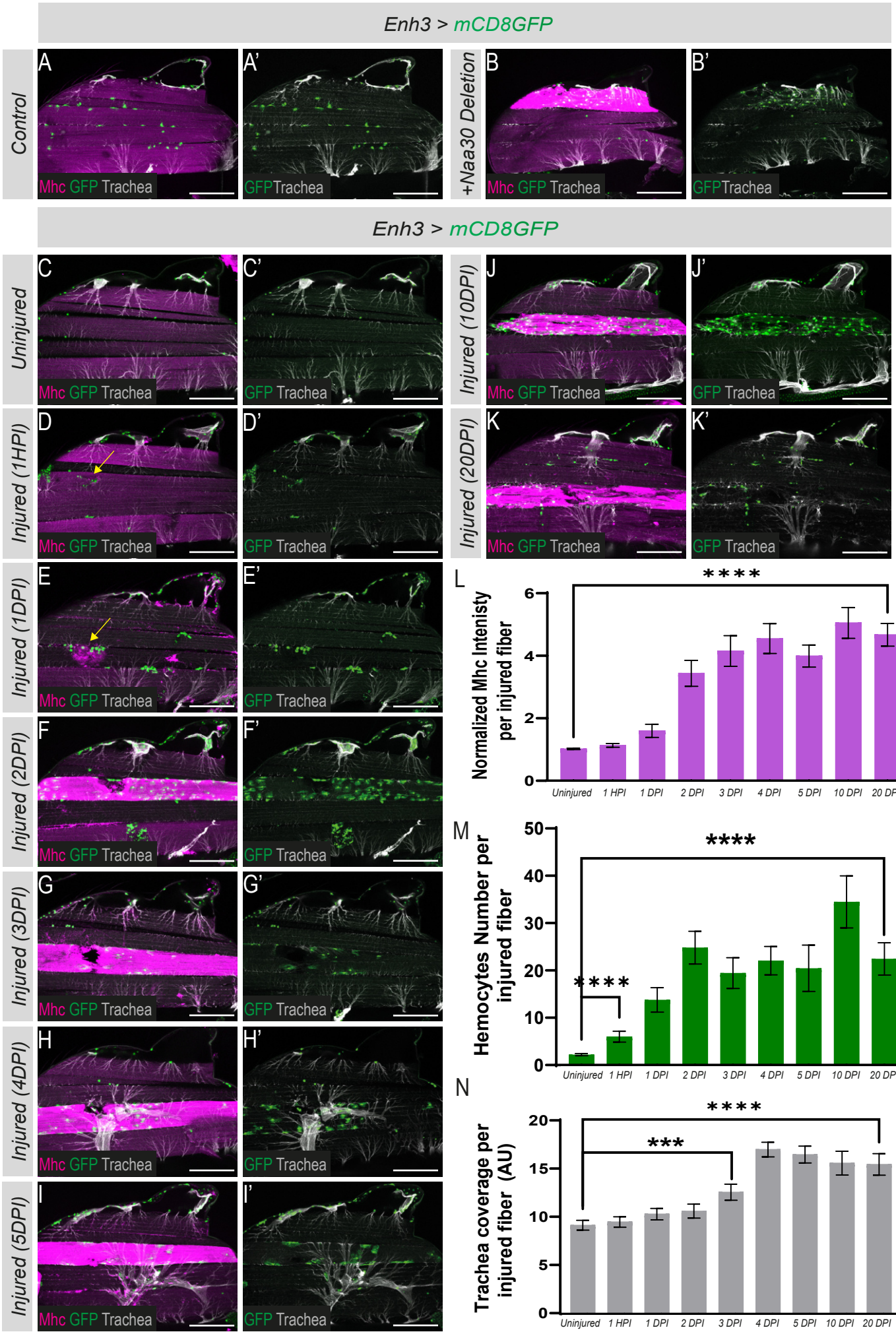
Enh3 > mCD8GFP
Control
+Naa30 Deletion
A
A'
B
B'
Mhc GFP Trachea
GFP Trachea
Enh3 > mCD8GFP
Uninjured
Injured (1HPI)
Injured (1DPI)
Injured (2DPI)
Injured (3DPI)
Injured (4DPI)
Injured (5DPI)
Injured (10DPI)
Injured (20DPI)
C
C'
D
D'
E
E'
F
F'
G
G'
H
H'
I
I'
J
J'
K
K'
L
Normalized Mhc Intenisty per injured fiber
****
Uninjured
1 HPI
1 DPI
2 DPI
3 DPI
4 DPI
5 DPI
10 DPI
20 DPI
M
Hemocytes Number per injured fiber
****
****
N
Trachea coverage per injured fiber (AU)
****
***

Figure S2

Figure S2. Early recruitment of hemocytes initiates tracheal remodeling after muscle damage. (A-B'). In *Naa30A mutant* flies, defective muscle attachment is associated with tracheal enrichment (gray, B') and increased hemocytes accumulation (green, B') compared to controls (A-A'). **(C-K').** Time-course analysis of tracheal remodeling and hemocytes recruitment in *Enh3-Gal4; UAS-mCD8GFP* adult IFMs following localized stab injury. Tracheal branches are visualized by autofluorescence (gray), and hemocytes are labeled with GFP (green). Muscles are labeled with Mhc (magenta). Time points range from 1-hour post-injury (1HPI) to 20 days post-injury (20DPI). **(L).** Quantification of normalized Mhc intensity. **(M).** Quantification of the hemocytes number in the injured fiber shows a significant increase starting at 1HPI which remains elevated until 20DPI. **(N).** Tracheal quantification shows a marked increase in its density from 3DPI and remains sustained until 20 DPI. (****$p < 0.0001$, ***$p < 0.001$; Student's t-test; $n \geq 10$ heminota per condition). Scale bars: 200 µm.

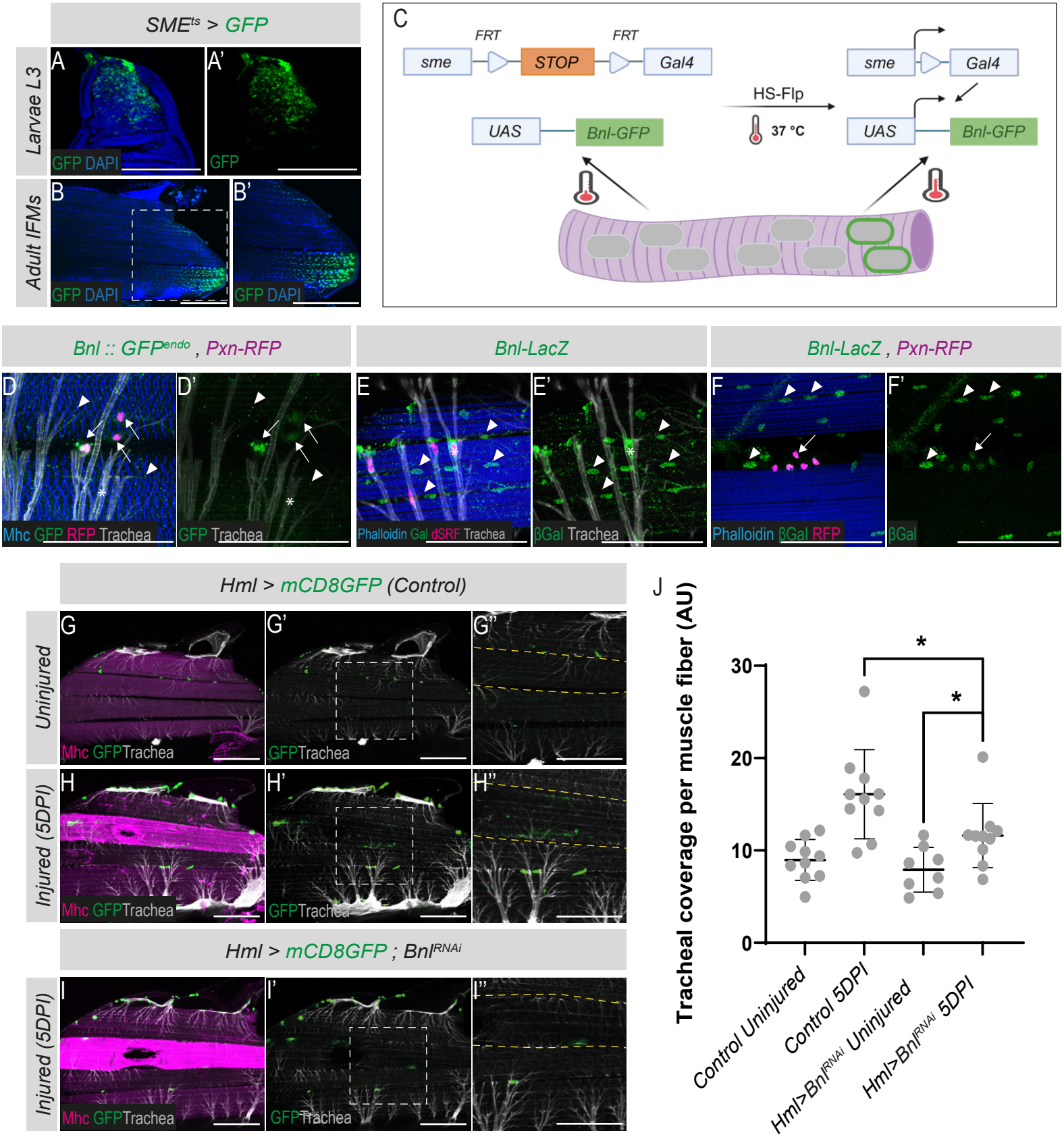
SMEts > GFP
Larvae L3
Adult IFMs
A
A'
B
B'
GFP DAPI
GFP
C
FRT
FRT
sme
STOP
Gal4
HS-Flp
37 °C
UAS
Bnl-GFP
Bnl :: GFPendo , Pxn-RFP
Bnl-LacZ
Bnl-LacZ , Pxn-RFP
D
D'
E
E'
F
F'
Mhc GFP RFP Trachea
GFP Trachea
Phalloidin Gal dSRF Trachea
βGal Trachea
Phalloidin βGal RFP
βGal
Hml > mCD8GFP (Control)
Uninjured
Injured (5DPI)
G
G'
G''
H
H'
H''
Mhc GFPTrachea
GFPTrachea
Hml > mCD8GFP ; BnlRNAi
I
I'
I''
J
Tracheal coverage per muscle fiber (AU)
30
20
10
0
*
*
Control Uninjured
Control 5DPI
HmlBnlRNAi Uninjured
HmlBnlRNAi 5DPI

Figure S3

Figure S3. Tracheal branching requires precise control of Bnl provided by the hemocytes. (A-B'). Expression pattern of the Shavenbaby (Svb) muscle regulatory enhancer (SME) (green, *SME-Gal4; UAS-mCD8GFP*). SME-Gal4 drives GFP expression (green) in a subset of larval muscle progenitors located in the posterior region of the wing disc (A-A') and in a subset of adult muscle nuclei (green and blue (DAPI), B-B'). Scale bars: 200 µm. **(C).** Schematic representation of the FLP-OUT system used to drive UAS-Bnl::GFP expression in a subset of adult muscle nuclei, using the *Hs-FLP; FRT-SME-Stop-FRT-Gal4/CyO; tub-Gal80ts* combination. **(D-D').** The endogenous Bnl (green, *Bnl::GFP*^{endo}) is detected in indirect flight muscles (IFMs, labelled with Mhc, blue; arrowheads), tracheal branches (autofluorescence, gray; asterisks), and hemocytes (*Pxn-RFP*, magenta; arrows). Scale bars: 25 µm. **(E-E').** Expression of the *Bnl-LacZ* reporter (green) is observed in terminal tracheal cells (TTCs) marked by dSRF (magenta; asterisks), and in IFMs nuclei (arrowheads). Scale bars: 25 µm. **(F-F').** Bnl-LacZ (green) is detected in IFMs associated hemocytes labelled with *Pxn-RFP* (magenta; arrows). Scale bars: 25 µm. **(G-I'').** Targeted downregulation of *bnl* in a subset of hemocytes using *HmlΔ-Gal4* driver significantly reduces tracheal enrichment at the injured fiber, as quantified in **(J).** (*$p < 0.05$, Student's t-test; $n \geq 10$ heminota per condition). Scale bars: 200 µm.

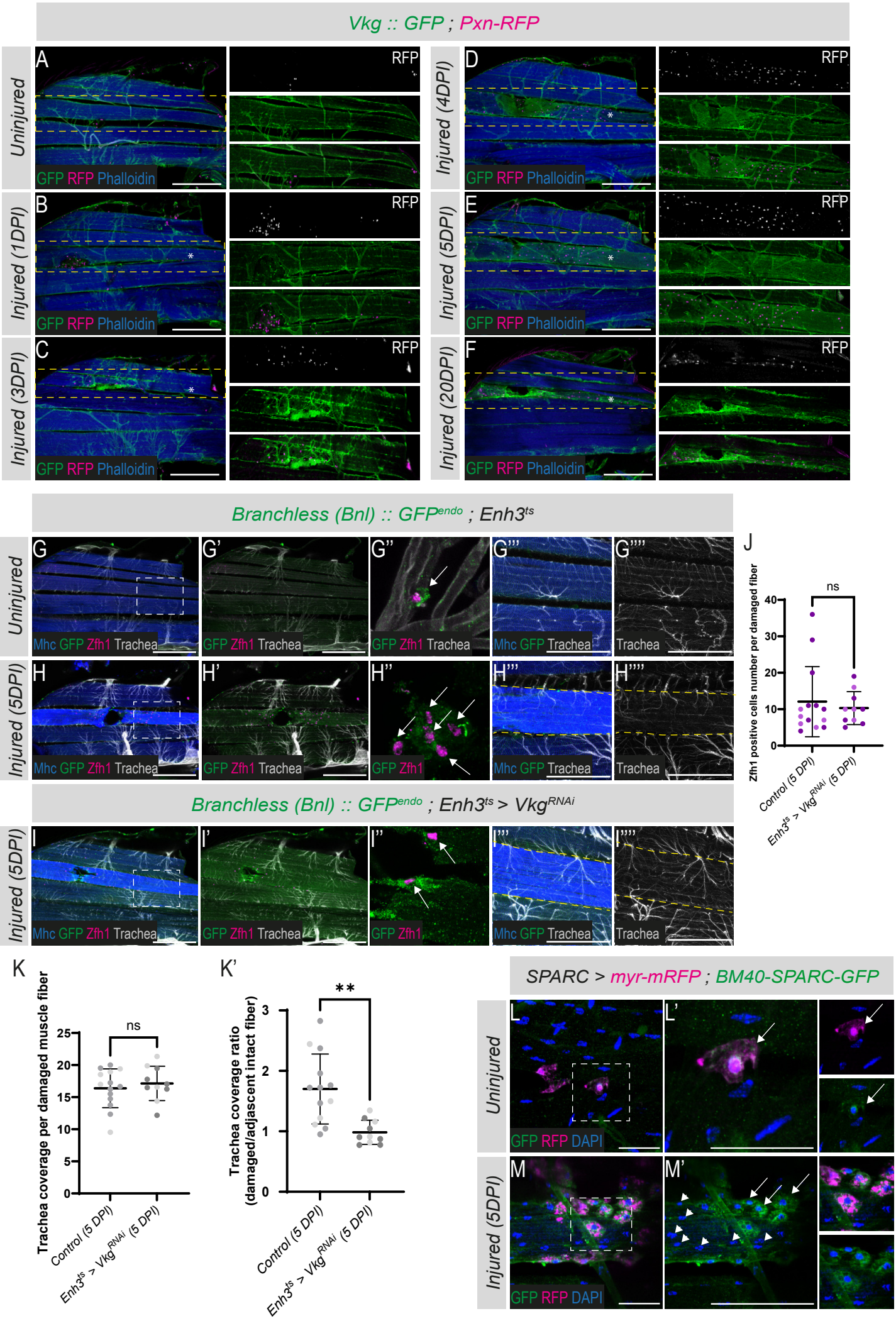
Vkg :: GFP ; Pxn-RFP
Uninjured
Injured (1DPI)
Injured (3DPI)
Injured (4DPI)
Injured (5DPI)
Injured (20DPI)
A
B
C
D
E
F
RFP
GFP RFP Phalloidin
Branchless (Bnl) :: GFPendo ; Enh3ts
G
G'
G''
G'''
G''''
H
H'
H''
H'''
H''''
Mhc GFP Zfh1 Trachea
GFP Zfh1 Trachea
GFP Zfh1
Mhc GFP Trachea
Trachea
J
Zfh1 positive cells number per damaged fiber
ns
Control (5 DPI)
Enh3ts > VkgRNAi (5 DPI)
Branchless (Bnl) :: GFPendo ; Enh3ts > VkgRNAi
I
I'
I''
I'''
I''''
K
Trachea coverage per damaged muscle fiber
K'
Trachea coverage ratio (damaged/adjascent intact fiber)
**
SPARC > myr-mRFP ; BM40-SPARC-GFP
L
L'
M
M'
GFP RFP DAPI

Figure S4

Figure S4. Analysis of hemocyte recruitment, Collagen IV deposition, and Bnl localization following muscle injury. (A-F). Hemocyte recruitment (magenta, *Pxn-RFP*) and Collagen IV distribution (green, *Vkg::GFP*) in uninjured muscles (A) and at successive time points after injury (B-F), from 1 to 20 DPI. Scale bar: 200 µm. **(G-G'').** The endogenous Bnl ligand (green, *Bnl::GFP^{endo})* is detected around the hemocytes labeled with Zfh1 (magenta, arrows). **(H-I'').** Depletion of Collagen IV in the hemocytes using *Enh3-Gal4 driver (Enh3-Gal4, UAS-Vkg^{RNAi})* does not affect Bnl production by hemocytes (green, Bnl::GFP^{endo}; arrows) nor their recruitment to injured fibers (Zfh1, magenta) as quantified in **(J)** (ns, Student's t-test; n ≥ 10 heminota per condition from two independent replicates). Scale bars: 200 µm. **(H'''-H'''' and I'''-I'''').** Hemocytes-specific knockdown of Collagen IV *(Enh3-Gal4, UAS-Vkg^{RNAi})* does not affect the trachea enrichment in the damaged fiber (Quantifications in **(K)** ns, Student's t-test; n ≥ 10 heminota per condition from two independent replicates). The ratio of tracheal enrichment in damaged fiber relative to adjacent non-injured fiber is significantly reduced upon *vkg* knockdown **(K')**. Scale bars: 200 µm. (**p<0.01, Student's t-test; n ≥ 10 heminota per condition from two independent replicates). **(L-M').** Muscle-associated hemocytes (arrows; round-shaped nuclei), but not muscle nuclei (arrowheads; flattened nuclei), express both the SPARC-Gal4, UAS-myr-RFP reporter (magenta) and BM40-SPARC-GFP (green) in uninjured and injured muscles. Nuclei are labelled with DAPI (blue). Scale bars: 25 µm.